Article:
Zhang, B, Yao, S, Mills, BJW orcid.org/0000-0002-9141-0931 et al. (6 more authors) (2020) Middle Permian organic carbon isotope stratigraphy and the origin of the Kamura Event. Gondwana Research, 79. pp. 217-232. ISSN 1342-937X

https://doi.org/10.1016/j.gr.2019.09.013

Middle Permian organic carbon isotope stratigraphy and the origin of the Kamura Event

Bolin Zhang[1], Suping Yao[1*], Benjamin J. W. Mills[2], Paul B. Wignall[2], Wenxuan Hu[1], Biao Liu[1], Yongle Ren[1], Lele Li[1], Gang Shi[3]

[1] *MOE Key Laboratory of Surficial Geochemistry, School of Earth Sciences and Engineering, Nanjing University, Nanjing 210023, China*

[2] *School of Earth and Environment, University of Leeds, Leeds LS2 9JT, UK*

[3] *Nanjing Geological Survey Center, China Geological Survey, Nanjing 210016, China*

**corresponding author: spyao@nju.edu.cn*

Abstract: Large carbon cycle perturbations associated with the Middle Permian (Capitanian) mass extinction have been widely reported, but their causes and timing are still in dispute. Low resolution carbon isotope records prior to this event also limit the construction of a Middle Permian chemostratigraphic framework and global or local stratigraphic correlation, and hence limit our understanding of carbon cycle and environmental changes. To investigate these issues, we analyzed the $^{13}C_{org}$ values from the Middle Permian chert-mudstone sequence (Gufeng Formation) in the Lower Yangtze deep-water basin (South China) and compared them with published records to build a chemostratigraphic scheme and discuss the underlying environmental events. The records show increased $\delta^{13}C_{org}$ values from late Kungurian to early Guadalupian, followed by a decrease to the late Wordian/early Capitanian. The early-mid Capitanian was characterized by elevated $\delta^{13}C_{org}$ values suggesting the presence of the "Kamura Event": an interval of heavy positive values seen in the $\delta^{13}C_{carb}$ record. We propose that these heavy Capitanian $\delta^{13}C$ values may be a response to a marked decline in chemical weathering

rates on Pangea and associated reduction in carbonate burial, which we show using a biogeochemical model. The subsequent negative $\delta^{13}C$ excursion seen in some carbonate records, especially in shallower-water sections (and in a muted expression in organic carbon) coincide with the Capitanian mass extinction may be caused by the input of isotopically-light carbon sourced from the terrestrial decomposition of organic matter.

Keywords: Guadalupian; Capitanian mass extinction; chemostratigraphy; Carbon cycle; Emeishan volcanism

1. Introduction

The Middle Permian (Guadalupian) represents a critical time in Earth history, marked by a mass extinction, major eruptions of large igneous province, a second-order, low-point in global sea-level and the cessation of Late Palaeozoic Ice Age (Jin et al., 1994; Zhou et al., 2002; Montañez et al., 2007; Wignall et al., 2009). Large carbon cycle perturbations associated with the late Middle Permian (Capitanian) mass extinction had been widely reported (Bond et al., 2010b; Isozaki et al., 2007a, b; Lai et al., 2008; Shen et al., 2013; Wang et al., 2004; Wignall et al., 2009; Yan et al., 2013), and variously attributed to collapse of biologic productivity (Wang et al., 2004; Isozaki et al., 2007a, b; Yan et al., 2013; Nishikane et al., 2014), development of ocean stratification and anoxia (Saitoh et al., 2013; Zhang et al., 2015), changes of sea-level (Wang et al., 2004; Lai et al., 2008; Wei et al., 2017), sudden release of methane (Retallack and Jahren, 2008; Bond et al., 2010a) and eruptions of Emeishan volcanism (Wignall et al., 2009; Bond et al., 2010b). However, the reported $\delta^{13}C$ trends vary considerably and this points to the need for more study before these conflicting interpretations can be better evaluated.

The Kamura event, which occurred in the Early-Middle Capitanian, has been interpreted as a

three-million-year long period of high productivity and enhanced burial of isotopically light organic carbon, that drew down atmospheric CO_2 resulting in a cool climate (Isozaki et al., 2007a, b, 2011). This event was originally confirmed by an exceptionally high positive inorganic carbon isotope excursion (+5 ‰) in the mid-Panthalassan Kamura paleo-atoll limestone in Japan (Isozaki et al., 2007a, b) and subsequently widely reported in equatorial Paleo-Tethys periphery marine carbonate (e.g., South China and Central Croatia) (Bond et al., 2010b; Isozaki et al., 2011; Cao et al., 2018). However, it is not clearly developed at the global stratotype section at Penglaitan (Guangxi Province) (Chen et al., 2011) which may just suggest a regional or diagenetic signal (Cao et al., 2018). Furthermore, its global significance is also questioned by the inconsistent $\delta^{13}C_{carb}$ records in South China (Cao et al. 2018). In addition, there is no evidence for global organic-matter deposition associated with this interval (Bond et al. 2010b), except in the northwestern margin of the Yangtze platform (e.g., Zhang et al., 2018). However, these organic-rich deposits could be caused by coastal upwelling (Zhang et al., 2018), which regionally developed along the western coasts of continents. Thus, the explanation that high primary productivity resulted in this high positive carbon isotope excursion and possible global-scale climatic cooling has also been questioned (e.g., Bond et al., 2010b; Cao et al. 2018).

A long-term problem in Middle Permian stratigraphic is the lack of a correlative framework that allows different regions and sites of different water depths to be compared at high temporal resolution. Deep-water facies are commonly biogenic cherts and their radiolarians provide a useful zonation scheme (e.g., Kametaka et al., 2009), but shallower facies are usually correlated using conodonts, that provide the highest resolution for the interval, or fusulinid forams in shallow, tropical limestones. Changes in the carbon isotopic composition of both carbonate and

organic matter can be used as a reliable tool for stratigraphic correlation (e.g., Weissert et al., 2008) and offers an alternative approach for correlating. Nonetheless, the Middle Permian carbon cycle perturbations remain poorly documented. The building of high-resolution carbon isotope chemostratigraphy can help determine the precise stratigraphic horizon/range of the Middle Permian and make the global correlations, which could further provide vital constraints on the nature of biotic crisis and geological change.

We have analyzed the $\delta^{13}C_{org}$ values from a Middle Permian chert-mudstone sequence (Gufeng Formation) in the Lower Yangtze deep-water basin, South China. This accumulated on the eastern margin of the Paleo-Tethys Ocean and faced onto the Panthalassa Ocean (Fig. 1a; e.g., Wang and Jin, 2000). Two outcrop sections and one drill core located in different sedimentary settings (lower slope, shallow shelf and inter-platform basin) were selected. These data, together with published records, have allowed the construction of a global carbon isotope curve for the Middle Permian. We attempt to resolve the uncertainty of possible causes concerning the nature of the Kamura event using a simple box modelling approach that suggests it may have a fundamentally different origin to previous suggestions. The different magnitudes and duration of the subsequent late Capitanian negative $\delta^{13}C_{org}$ excursions which related with the Captianian mass extinction are also discussed.

2. Geological setting

2.1 Paleogeographic setting

During the Middle Permian, the South China craton was located close to the palaeo-equator in the eastern Paleo-Tethys Ocean (Fig. 1a, Wang and Jin, 2000). A large northeast-southwest trending shallow water carbonate region, known as the Yangtze Platform, occurred in its central

part and was surrounded by deep-water basins (Fig. 1b). The Lower Yangtze deep-water basin, saw widespread, black chert-mudstone rhythms accumulate (Gufeng Formation), and was situated on its northwestern margin (present-day north, Fig.1b) and is thought to have experienced intense, periodic ocean upwelling (Kametaka et al. 2005; Yao et al. 2015; Zhang et al., 2018). The Gufeng (Kuhfeng) Formation is underlain by the Qixia (Chihsia) Formation, a shallow-marine limestones of Early Permian (Cisuralian) age (Fig. 2), and overlain by the Yinping Formation, a coastal, clastic deposit (shale and siltstone) of late Middle Permian (Capitanian) age (Bureau of Geology and Mineral Resources of Anhui Province 1989; Kametaka et al. 2005).

2.2 Study sections

Two well-exposed sections (Pingdingshan and Qinglongshan) and one newly-drilled core (Gangdi) were chosen for this study to provide stratigraphic, and chemostratigraphic correlation in the Lower Yangtze region during the Guadalupian. The Pingdingshan (PDS) section is located on the north limb of the Pingdingshan syncline in the Chaohu area (GPS 31°37′51.5″ N, 117°49′21.8″ E, Fig. 1c) and contains a complete record of Middle Permian strata (Fig. 2). It consists of chert and siliceous mudstone of the Gufeng Formation and shale of the overlying Lower Yinping Formation, both were deposited in an open-marine, lower slope setting (Kametaka et al. 2005, 2009). The Gufeng Formation unconformably overlies the shallow-marine limestones of the Qixia (Chihsia) Formation, and is continuously succeeded by the Yinping Formation. The Gufeng Formation is subdivided into three members — the Lower Phosphate Nodule-bearing Mudstone Member (LPMM), the Middle Chert-Mudstone Member (MCMM) and the Upper Mudstone Member (UMM) (Zhang et al., 2019). The basal beds of the Gufeng Formation in the Chaohu area contain conodonts (*Jinogondolella nankingensis*, Kametaka et al., 2009) and ammonoids

(*Nodogastrioceras discum*, Wu et al., 2017; *Erinoceras sp*, Kametaka et al., 2009). Three radiolarian assemblage zones have also been established in the Gufeng Formation which indicate a Roadian-Capitanian age (Kametaka et al., 2009). In addition, two tuffs from the bottom and topmost part of the Gufeng Formation at this section have yielded zircons which have provided U-Pb ages of 272.95 ± 0.11 Ma (dated by CA-ID-TIMS technique, Wu et al., 2017) and 261.6 ± 1.6 Ma (dated by LA-ICP-MS technique, Zhang et al., 2019) respectively, indicating that Gufeng deposition lasted about 11 Ma (Fig. 2). Thus, this well-studied section with good biostratigraphic controls and radio-isotopic ages, provides an excellent deep-water reference section for the Guadalupian of the study area, with absolute age constraints that can be used to date a chemostratigraphic record.

Located on the north limb of the Longtan-Baohuasha syncline in the Nanjing area (GPS 32°09′42.2″ N, 119°04′54.6″ E, Fig. 1c), the Qinglongshan (QLS) section exposes a complete section of Early-Middle Permian strata (Fig. S1). Compared with the Pingdingshan section, the Gufeng Formation has a relatively thin chert-mudstone sequence with a thickness of about 7m. However, the Gufeng Formation facies are the same: a deep-water, black chert and siliceous mudstone succession that can be subdivided into three members (Fig. 2). The Yinping Formation is approximately 37 m thick and composed of grey to grey-black shale and silty mudstone (Fig. 2) that was deposited in a nearshore setting of the Lower Yangtze region.

The Gangdi (GD) core, drilled by the Nanjing Institute of Geology and Mineral Resources, is in Ningguo City (Fig. 1c), ~140 km southeast of Chaohu City and located in an epicontinental basin within the Yangtze Platform (Fig. 1c). The Gufeng Formation mainly consists of black chert and siliceous mudstone and its three lithological members can be recognized (Fig. 2). The Yinping

Formation is characterized by black to pale-grey mudstone, shale and siltstone.

3. Samples and methods

A total of 193 fresh and unweathered samples, including chert, siliceous mudstone and shale, were collected from these sections, and pulverized to 200 mesh in an agate mortar and pestle for geochemical analysis. Total organic carbon (TOC), total nitrogen (TN) and total sulphur (TS) contents were measured using an Elementar® Vario MACRO CHNS elemental analyzer at the Key Laboratory of Surficial Geochemistry of the Ministry of Education, Nanjing University. All samples were treated with 2 M HCl for 24 h to remove inorganic carbon, washed to neutral and dried for the final measurements on the machine. Analytical precision for TOC, TN and TS contents is better than 1 %, 5 % and 5 %, respectively. Al concentrations were determined by wavelength-dispersive X-ray fluorescence spectrometry (XRF) technique on fused glass sheets and carried out using an ARL9900 XRF with analytical precision better than 1 % at the State Key Laboratory for Mineral Deposits Research, Nanjing University.

For organic carbon isotopes, all the powdered samples were decarbonated using 4 M HCl for > 24 hours until effervescence ceased. Then the residue was separated by repeated centrifugation and washed with distilled water until neutrality was reached. After drying, samples were placed in tin cups and their $\delta^{13}C_{org}$ value was measured using continuous flow-elemental analysis-isotope ratio mass spectrometry, with a ThermoFinnigan Deltaplus Advantage mass spectrometer coupled with an EA 1112 Series Flash Elemental Analyzer at the State Key Laboratory for Mineral Deposits Research, Nanjing University. Analytical precision and reproducibility for $\delta^{13}C_{org}$ were checked by replicate analyses of international standards (USGS 40) and found to be better than 0.2 ‰. All stable carbon isotope data were reported in standard δ–

notation relative to the Vienna Peedee Belmnite (V-PDB) standard.

In order to gain a better understanding of the source input of organic matter in sediments, a total of 31 samples (15 from PDS section, 11 from QLS section, and 5 from GD core) have been prepared for palynofacies analysis following standard techniques (cf. Traverse, 2007). All samples were treated with concentrated hydrochloric and hydrofluoric acids to remove carbonates and silicates. No oxidative chemicals were applied to any of the residues. The residues were sieved using 10 µm nylon meshes and mounted on slides for subsequent microscopic analysis. For each palynological slide a minimum of 200 particles was counted for the quantitative analysis and classified into varieties of amorphous organic matter (AOM), phytoclasts and palynomorphs. The classification of organic matter particles follows the scheme proposed by Tyson (1995).

4. Results

4.1 Organic carbon isotopes

The Guadalupian $\delta^{13}C_{org}$ records from PDS section, GD core, and QLS section (see Table S1 and Figure 3) display a series of negative and positive shifts of up to 6 ‰. Correlation of the three records is possible because the sections show reasonably consistent changes. Here we subdivided these curves into 4 chemostratigraphic intervals (1-4) with three negative excursions (N1-N3) and three positive excursions (P1-P3) based on marked shifts and trends observed in the $\delta^{13}C_{org}$ record (Fig. 3). Interval 1 comprises the topmost metres of the Qixia Formation, and is characterized by $\delta^{13}C_{org}$ values around -27.5 ‰ (N1). The boundary between interval 1 and 2 is marked by a positive shift of about 2-2.5 ‰ (P1) that correlates with a possible unconformity between the Qixia and Gufeng Formations, and corresponds to an abrupt change in lithology from grey limestone to black mudstone. Interval 2 spans the basal part of the Gufeng Formation

(LPMM to middle MCMM), and is characterized by negatively trending $\delta^{13}C_{org}$ values that decrease from -25.5 to -28 ‰ (N2) and one positive $\delta^{13}C_{org}$ peak (P2) in the top of the interval. Interval 3 observed from the upper MCMM to UMM, is represented by a continued positive trend to $\delta^{13}C_{org}$ values around -26 ‰ to -25 ‰ (P3) before they gradually decrease again to values around -27 ‰ to -26 ‰ (N3), and can be further divided into two intervals (3a and 3b). Interval 3a is characterized by gradually increasing $\delta^{13}C_{org}$ values from around -26 ‰ to -25 ‰ and a small negative $\delta^{13}C_{org}$ excursion at its top. Interval 3b begins with a small positive $\delta^{13}C_{org}$ excursion and then shows a negative trend of $\delta^{13}C_{org}$ values (N3). Interval 4 shows a gradual, rising trend of $\delta^{13}C_{org}$ values (P3) in the highest part of the study sections, increasing from around -26.5 ‰ to -24 ‰.

4.2 Other geochemistry results

The TOC, TN, TS and Al contents of the Qixia Formation all maintain low values in our studied sections, but are variable in both Gufeng and Yinping Formation (Table S1 and Figs. 4). The TOC, TS contents and TS/TOC ratios in both the Gufeng and Yinping Formation of the PDS section had been reported by Zhang et al. (2019). In this section, the TN content ranges from 0.47 % to 1.24 % with an average of 1.0 % in the Gufeng Formation, but abruptly decreases in the LSM of the Yinping Formation (Fig. 4a). The Al contents are very low (mean 2.21 %) in both MCMM and UMM of the Gufeng Formation but higher in the LPMM (mean 5.26 %). The Al content increases rapidly from the bottom of the LSM to the MSM of the Yinping Formation, and then remains at a high level (Fig. 4a). TOC/TN ratios, ranging from 0.64 to 21.04 (mean 10.13), are very low in both Qixia and Yinping Formation, but abruptly increase to very high values in Gufeng Formation.

The GD core has gradually increased TOC, TS, TN and Al contents in the Gufeng Formation but with markedly variable values (Fig. 4b). The Yinping Formation in the GD core also shows abruptly decreased TOC contents and rapidly increased TS contents in the LSM, and these remain as relatively low values in the MSM (Fig. 4b). The Yinping Formation has increased Al concentration in the LSM and has higher values in its MSM (Fig. 4b). Markedly variable TS/TOC ratios are seen in the Gufeng Formation and most of them in the upper half of the Gufeng Formation are higher than ratios found in modern, normal marine settings. The Yinping Formation also has very high TS/TOC ratios > 0.36. The TOC/TN ratios range from 0.25 to 11.36 with a mean value of 4.61 in the GD core.

In the QLS section, extremely high TOC contents, relatively high TN contents, relatively low Al contents and very low TS contents are seen in the LPMM and MCMM of the Gufeng Formation (Fig. 4c). The overlying UMM has relatively decreased TOC contents, constant TN contents, and rapidly increased TS and Al contents (Fig. 4c). Also, the LSM of Yinping Formation has abruptly increased TS contents and relative low TOC contents (Fig. 4c). An abrupt decrease of Al concentration occurred in the bottom of LSM and then rapidly recovered to high values (Fig. 4c). TS/TOC ratios are relatively low in the LPMM and MCMM of the Gufeng Formation but higher than ratios of modern normal marine settings (~0.36) in the UMM and Yinping Formation (Fig. 4c). TOC/TN ratios, ranging from 0.04 to 17.18 with an average of 3.58, are very low in Qixia Formation, but abruptly increase to relatively high values in both Gufeng and Yinping formations.

4.3 Palynofacies data

The palynofacies data recorded from samples of our three studied sections are summarized in Table S2 and illustrated diagrammatically in Fig. 5. Examples of representative palynofacies

components are illustrated in Fig. 6. AOM is the most common structureless organic matter particles, most of which have a granular appearance with angular to sub-angular outlines (Fig. 6 a-e, i, n, o) while others show indistinct or diffused margins (Fig. 6 h, j, m). The phytoclasts are characterized by moderately preserved fragments with sharp angular edges and consist mainly of elongated, lath-shaped and unstructured woody tissues and debris (Fig. 6 f, g, j-l, p). Palynomorphs are scarce and mainly contains spores (Fig. 6 f, g). Most of these organic matter particles are dark brown or black in color (Fig. 6), which may be resulted from the high thermal maturity (mature to over-mature) in response to regional burial.

In all three studied sections, both the top Qixia Formation (Fig. 6 a, b, h, m) and the Gufeng Formation (Fig. 6 c-e, i-k, n-o) is marked by high proportion of AOM and comparatively low phytoclasts contents (Fig. 5). Palynomorphs are almost completely absent in nearly all of these samples (Fig. 5). In the lower Yinping Formation, phytoclasts (Fig. 6 f, g, l, p) begin to increase in most of the samples whereas palynomorphs (e.g., spores, Fig. 6 f, g) are also found to be present in low quantities (Fig. 5). Although some AOM can be formed as a result of intense degradation and fragmentation of woody tissues of higher plant, typical AOM is mostly derived from phytoplankton or is of bacterial origin (Tyson, 1995), suggesting a predominance of marine organic matter source. Phytoclasts and palynomorphs indicate a mainly terrestrially-derived organic matter source. Based on these palynofacies observations, we found that both the top Qixia and Gufeng Formation is dominated by marine organic matter source, whereas the lower Yinping Formation is characterized by a complex mixture of marine and terrigenous source.

5. Discussion

5.1 Source of organic matter and diagenetic influence

Bulk organic carbon isotopic composition of marine sediments can provide a global signal but it is also affected by the changing contributions of terrestrial and marine organic carbon (Meyers, 1997; Hayes et al., 1999), thermal maturation (Hayes et al., 1999) and diagenetic changes during degradation (Hayes et al., 1989). When attempting to get an original Permian $\delta^{13}C$ signal it is therefore important to evaluate the factors that contribute to it.

During the Late Paleozoic era, marine and terrestrial organic matter had different ranges of carbon isotope values to today (Arthur et al., 1985), with ranges of -25 ‰ to -30 ‰ for marine organic matter (e.g., Grasby and Beauchamp, 2008; Luo et al., 2014) and -22 ‰ to -24 ‰ for terrestrial organic matter (e.g., Strauss and Peters-Kottig, 2003; Thomas et al., 2004; Hermann et al., 2010). In the Qixia Formation the light $\delta^{13}C_{org}$ values (mean -27.5 ‰) and near absence of siliciclastic input (indicated by low Al contents with mean values < 0.3 %) (Fig. 4) suggest that these Lower Yangtze platforms carbonate facies contain little or no terrigenous organic matter and so record a primary marine $\delta^{13}C_{org}$ signatures (e.g., Luo et al., 2014). This is also confirmed by our palynofacies analysis (Fig. 5), which indicates a mainly marine-derived source.

Samples of Gufeng Formation also show relatively low bulk $\delta^{13}C_{org}$ values (-28 to -25 ‰), and high TOC values (Fig. 4), indicating that the chert-mudstone rhythms contain a larger proportion of marine organic matter. This is supported by organic petrography observations that show the organic matter is primarily amorphous organic matter (Figs. 5 and 6) with a likely marine planktonic origin (Liang et al., 2009). The low terrigenous input in the Gufeng Formation is further indicated by low Al values of 2.6-4.8 %. Furthermore, there is no significant correlation

between Al and $\delta^{13}C_{org}$ in these sections (R^2 = 0.28, 0.30, 0.28; Fig. 7b, e, h), suggesting that changes in terrestrial organic matter flux had a negligible influence on the bulk $\delta^{13}C_{org}$ values. Thus, we can reasonably infer that the Gufeng Formation organic matter was predominantly of marine origin.

The Yinping Formation of the PDS section is characterized by heavier bulk $\delta^{13}C_{org}$ values, higher siliciclastic inputs (Fig. 4a), and possible correlation of Al and $\delta^{13}C_{org}$ (R^2 = 0.83; Fig. 7b) suggesting significant terrestrial organic carbon input. The increase of terrestrial carbons could have resulted in the positive excursion of the $\delta^{13}C_{org}$ values. This is especially the case in the Yinping Formation of both the GD core and QLS section which have varying but heavy $\delta^{13}C_{org}$ values, high siliciclastic inputs (Fig. 4) and phytoclasts contents (Fig. 5), and is likely due to their more proximal setting. Variable mixing of marine and terrestrially derived organic matter in the lower Yinping Formation (Fig. 5) could have obscured the global carbon isotope signature, despite the insignificant correlation of Al and $\delta^{13}C_{org}$ (R^2 = 0.05 and 0.12; Fig. 7d, f).

TOC/TN ratios have been widely used to distinguish marine and terrestrial organic matter, although they can be influenced by both diagenesis and remineralization in the water-column and sediment (e.g., Meyers, 1997). Marine organic matter normally has low TOC/TN ratios of $\leqslant$ 10, whereas terrestrial organic matter typically have TOC/TN ratios of $\geqslant$ 20 (Meyers, 1997). The TOC/TN ratios in both GD core and QLS section predominantly fall between 0 and 10, suggesting marine organic matter. Samples with low TOC/TN ratios ($\leqslant$ 10) in the PDS section indicate a marine source, whereas other elevated TOC/TN ratios (ranging from 10 to 20), probably indicate a minor terrestrial influence. However, the good linear correlations between TOC and TOC/TN of our three studied sections (R^2 = 0.63, $p(\alpha) < 0.01$ for PDS section; R^2 = 0.80, $p(\alpha) < 0.01$ for GD

core; and R^2 = 0.99, p(α) < 0.01 for QLS section; Fig. S2) indicate the preferential loss of organic N from sediments during diagenesis and/or thermal metamorphism (e.g., Wang et al., 2015), which could also cause these higher values. Furthermore, these relatively high TOC/TN ratios ranging between 10 and 20, could also be attributed to enhanced preservation of organic carbon or preferential degradation of nitrogen-rich components under depleted oxygen conditions (Twichell et al, 2002). With no evidence of conspicuous terrestrial inputs (i.e., low Al contents), we envisage a scenario of mostly marine-sourced organic matter produced in an intensive upwelling system along the northwest margin of South China (Zhang et al., 2018). As shown in figure 7, the relationship between TOC/TN ratios and $\delta^{13}C_{org}$ values in our three studied sections indicates that the major source of the organic matter was marine. Additionally, the poor relationship between $\delta^{13}C_{org}$ and TOC/TN of our studied sections (R^2 = 0.13, 0.11, and 0.01, respectively; Fig. 7) further suggest that the temporal variations of $\delta^{13}C_{org}$ are not caused by changes of organic matter source.

Thermal maturation and degradation of labile organic compounds can cause a decrease of the total organic carbon content and increases the $\delta^{13}C$ values of the residual TOC (Hayes et al., 1999). However, this process does not alter the trends recorded by the $\delta^{13}C_{org}$ values (Des Marais et al., 1992). Furthermore, the data show no strong correlation between TOC and $\delta^{13}C_{org}$ values (Fig. 7a, d, g), suggesting that diagenetic effects have not greatly influenced the isotopic trends (e.g., Hayes et al., 1989).

5.2 Guadalupian $\delta^{13}C_{org}$ chemostratigraphy and global correlation

The data obtained here are compared with a compilation of published $\delta^{13}C$ records of both carbonate and organic matter that span the late Early Permian to early Late Permian interval

from numerous regions in order to build a global, chemostratigraphic record. This shows that the late Kungurian saw a major increase in $\delta^{13}C_{carb}$ values (3 ‰) that produced an interval of heavy values (~4 ‰) which persisted (with secondary fluctuations) for much of the Guadalupian in several records (Fig. 8). Superimposed on this heavy plateau of values, $\delta^{13}C_{carb}$ values in South China (e.g., Naqing section) show two positive excursions in the lower Roadian and the Roadian-Wordian boundary (R-WB) (Buggisch et al., 2011) separated by a negative excursion within the Roadian. Although Wordian $\delta^{13}C_{carb}$ values have not been studied in detail, an upper negative shift from the positive peak at the R-WB (Buggisch et al., 2011; Korte et al., 2005; Nishikane et al., 2014) could have occurred in this stage and then rapidly recovered in the late Wordian/early Capitanian (Korte et al., 2005).

The P1 positive excursion which occurred in the boundary between the Qixia and Gufeng Formations, was best dated by its boundary tuff with U-Pb ages of 272.95 ± 0.11 Ma (Wu et al., 2017), suggesting an early Roadian interval, whereas the N2 negative excursion corresponds to the appearance of *J. nankingensis* conodonts, the whole *Pseudoalbaillella (P.) longtanensis–P. fusiformis* zone (Roadian-Wordian), and most of the *Follicucullus monacanthus* zone (Wordian-early Capitanian) (Kametaka et al., 2009), suggesting a Roadian-Wordian interval. The variations of our $\delta^{13}C_{org}$ values in all three sections are in accordance with these records (Fig. 8), suggesting a consistent carbon cycling and perturbation in the Roadian-Wordian interval. It could be argued that these single point positive excursions in the middle of Interval 2 of our three studied sections are insufficient to indicate a trend. Alternatively, they could represent a carbon perturbation at the R-WB, coincident with the appearance of the *Follicucullus monacanthus* zone (Wordian-early Capitanian) (Kametaka et al., 2009). The subsequent negative trend, was within

the *Follicucullus monacanthus* zone, in our three studied sections (Fig. 8) can be tentatively correlated with these Wordian $\delta^{13}C_{carb}$ trends.

The early-mid Capitanian is characterized by widely reported, elevated $\delta^{13}C$ values with positive peaks in both carbonate and organic matter (Isozaki et al., 2007a, b; Bond et al., 2010b; Birgenheier et al., 2010; Nishikane et al., 2014; Cao et al., 2018) that have been called the 'Kamura Event' by Isozaki et al. (2007a, b). The onset of this event is clearly seen in numerous sections (Fig. 8), and is the heaviest interval of $\delta^{13}C_{carb}$ values seen in the entire Phanerozoic (Gradstein et al. 2012). Its termination was originally proposed to be characterized by a negative inflexion at the end of the Capitanian (Isozaki et al., 2007a, b). Our $\delta^{13}C_{org}$ records reported here also shows a trend of increasing $\delta^{13}C_{org}$ values with positive spike (P2, Fig. 8), indicating a consistent global carbon cycling during the early-middle Capitanian. Based on radiolarian biostratigraphy, the P2 positive excursions occurred at the upper part of *Follicucullus monacanthus* zone and throughout the *Follicucullus scholasticus–Ruzhencevispongus uralicus* (early-middle Capitanian) zones (Kametaka et al., 2009), indicating an early-middle Capitanian interval carbon perturbation.

A major negative shift in $\delta^{13}C_{carb}$ values of 3-7 ‰ followed this Kamura Event has been reported from the middle Capitanian of western Guizhou (Bond et al., 2010b; Wignall et al., 2009), western Hubei (Cao et al., 2018) and northern Sichuan (Shen et al., 2013; Jost et al., 2014), and negative excursions in $\delta^{13}C_{org}$ are also seen in Japan (Nishikane et al., 2014), eastern Australia (Birgenheier et al., 2010), Spitsbergen (Bond et al., 2015) and central Korea (Kwon et al., 2018), although the magnitude and possibly the detailed timing of these excursions varies considerably (Shen et al., 2013; Jost et al., 2014). However, this negative excursion is not seen in all sections in

South China (e.g., Penglaitan section; Wang et al., 2004) nor in Hungary and Greece (Wignall et al., 2012). The different magnitudes and duration of this negative $\delta^{13}C_{carb}$ shifts may be due to local effects or diagenetic alteration, which could have significantly altered the original carbon isotope signal of seawater (Jost et al., 2014), and stratigraphic hiatuses, which could have caused its absence in many sections. Furthermore, Jost et al. (2014) and Bagherpour et al. (2018) suggested that these inconsistent changes of $\delta^{13}C_{carb}$ across sections favour local changes rather than a global carbon cycle event but rather local changes, with the low values affected by subaerial exposure and meteoric alteration.

A chemostratigraphic correlation scheme using $\delta^{13}C_{org}$ isotope values from marine and terrestrial records from various areas for the Capitanian stage have been well established on the basis of their biostratigraphy and tuff radiometric dating, which provide us a window to better understand the carbon isotope cycle and perturbation. As shown in figure 9, the most distinct, common feature of these carbon isotope records is the negative shift close to the Capitanian extinction event and the eruption of the Emeishan flood basalts. These relatively consistent negative excursions also show variable magnitudes with smaller negative shift for deep-water facies (⩽1 ‰, e.g., Gujo-hachiman section) and larger for relatively shallow-water facies (2-3 ‰, e.g., Kapp Starostin section). Notably, our new $\delta^{13}C_{org}$ records in the Lower Yangtze basin also exhibit a progressive basinward decrease in magnitude of ^{13}C shift (Figs. 3 and 8). This intrabasin trend was also reported for $\delta^{13}C$ excursions during the end-Permian (Grasby and Beauchamp, 2008) and end-Triassic mass extinction (Ruhl et al., 2009), and may be related to changes in the mixing ratio of organic matter sources or diagenetic remineralization of organic carbon. Thus, it could be argued that this may not really record a global signal that has been modified by local

and/or regional processes. However, our palynofacies analysis and the poor relationship between $\delta^{13}C_{org}$ and TOC/TN as discussed above (Fig. 7) suggests that the temporal variations of $\delta^{13}C_{org}$ are not solely caused by changes of organic matter source. More importantly, variable input of organic matter in different environmental settings only appears to affect the minimum values recorded and does not alter the record of the larger background global shift in $\delta^{13}C_{org}$ (Grasby and Beauchamp, 2008). Furthermore, $\delta^{13}C_{org}$ fluctuation could have also occurred earlier and stronger in shallow and/or near-shore environment than deeper (e.g., Arthur et al., 1985; Wang et al., 2004; Grasby and Beauchamp, 2008) due to the severe fluctuated carbon cycle that links ecosystem. This can be further testified by the terrestrial record at the Danyang section (Kwon et al., 2018), which shows significantly larger shifts (~6 ‰) than marine records (<3 ‰). Thus, the world-wide discrepancy of $\delta^{13}C_{org}$ between deep-water and shallow-water sediments can be also explained by such conditions and may reflect a global carbon cycle perturbation. Despite Jost et al. (2014) and Bagherpour et al. (2018) doubts about the reliability of these negative excursions as a primary signal, most previous studies have argued for a global negative excursion in $\delta^{13}C$ during the late Guadalupian (e.g., Bond et al., 2010b, 2015; Cheng et al., 2019; Isozaki et al., 2007; Lai et al., 2008; Saitoh et al., 2013a; Wang et al., 2004; Wei et al., 2012, 2017; Wignall et al., 2009a; Yan et al., 2013). According to our new data, the relatively consistent negative excursions, albeit with different magnitudes, is likely a global signal but influenced by local effects.

Followed this negative excursion, $\delta^{13}C$ values increased with a rapid positive shift of 4-6 ‰ and gradually continued to end-Capitanian (Bond et al., 2010b; Shen et al., 2013). A similar $\delta^{13}C$ shifts with different magnitudes shown in our own data (N3 and P3, Fig. 8) and other global sections (e.g., Xiongjiachang and Gouchang sections, Wignall et al., 2009; Bond et al., 2010b)

suggest a comparable carbon isotope cycle and perturbation during the middle–late Capitanian. In addition, dated tuff with U-Pb ages of 261.6 ± 1.6 Ma (Zhang et al., 2019) suggest that the N3 negative excursion occurred close to the middle Capitanian, whereas the P3 positive excursion was in the middle-late Capitanian.

5.3 Assessing causes of the Capitanian positive $\delta^{13}C$ excursion (Kamura Event)

Our studied sections show a progressive increase of $\delta^{13}C_{org}$ values, with positive excursions (P2), in the early-middle Capitanian (Fig. 8), which indicates that the Kamura Event is also seen in the organic carbon record. Potentially, elevated $\delta^{13}C_{org}$ values can be caused by increased terrestrial input but this does not appear to be the case here because there is a weak relationship between $\delta^{13}C_{org}$ and Al (Fig. 7b, d, f). Although our positive $\delta^{13}C_{org}$ excursion comes from the exceptionally organic-rich sediments of the Gufeng Formation (TOC contents > 10 %) which were developed beneath a zone of upwelling on the northern margin of the South China continent (Zhang et al. 2018), the Capitanian interval is not marked by globally extensive black shale deposition (Bond et al. 2010b). This regionally elevated TOC accumulation, is unlikely to have been responsible for a large and prolonged, global $\delta^{13}C$ excursion. Alternatively, Cao et al. (2018) argued that the positive excursions of $\delta^{13}C_{carb}$ seen in Capitanian carbonates of South China were attributable to local eutrophication effects fertilized by the weathering of the Emeishan flood basalts that were being erupted in the region at this time. They further noted a non-synchrony of the $\delta^{13}C_{carb}$ positive excursions, because their example, from Hubei Province, is restricted to the early *Jinogondolella prexuanhanensis* Zone, whilst the excursion begins earlier in the Capitanian in other sections (Bond et al. 2010b). Our $\delta^{13}C_{org}$ data show a prolonged period of heavier values throughout the Capitanian, with a positive excursion superimposed on the plateau

in interval 5 (P4) around the *J. prexuanhanensis* Zone (Fig. 8).

Clearly, there are issues with the both the origin and timing of the Kamura Event. Nonetheless there is clear evidence that the Capitanian interval was marked by exceptionally heavy $\delta^{13}C$ values (Fig. 8) indicating that it was not attributable only to local effects in South China as proposed by Cao et al. (2018). The original explanation for the positive excursion follows a well-known pathway and ascribes elevated productivity and enhanced organic carbon burial as the cause of the shift to heavy $\delta^{13}C$ values (Isozaki et al. 2007a, b). Global productivity levels are strongly influenced by run-off (and nutrient influx) which can be reflected in elevated $^{87}Sr/^{86}Sr$ values, but the Middle Permian interval in fact saw the lowest $^{87}Sr/^{86}Sr$ values of the Phanerozoic (Bond et al. 2015). The combination of exceptionally heavy $\delta^{13}C$ values and exceptionally low $^{87}Sr/^{86}Sr$ values therefore requires a different explanation. One possibility is that the tropically-emplaced Emeishan flood basalt underwent rapid chemical weathering, delivering high quantities of phosphorus and unradiogenic strontium to the ocean, which would stimulate productivity and act to lower seawater $^{87}Sr/^{86}Sr$. However, the Emeishan flood basalt had a relatively small weatherable area when compared to other LIPs (Ernst, 2014). For example, it is more than 10 times smaller in area than the ~200 Ma equatorially-emplaced Central Atlantic Magmatic Province (CAMP), and thus it seems unlikely that its effect on the marine Sr isotope budget was on a par with that of the CAMP (e.g., McArthur et al., 2012). Given that there is also no clear sedimentary evidence for globally-enhanced organic carbon burial during the Kamura event (Bond et al. 2010b), Emeishan flood basalt weathering can be ruled out as a major driver of the combined $^{87}Sr/^{86}Sr$ and $\delta^{13}C$ excursions.

An alternative hypothesis is explored here based on changes to the inorganic carbon cycle: It

has been shown that changes to carbonate weathering and deposition fluxes constitute an independent control on seawater $\delta^{13}C$ ratios, and thus a reduction in global erosion and sedimentation rates may drive a positive $\delta^{13}C$ excursion, evidenced by long-term inverse correlation between Phanerozoic $\delta^{13}C$ and $^{87}Sr/^{86}Sr$ records (Shields and Mills 2017). The Middle Permian marked the accretion of the Pangean supercontinent (e.g., Yin and Song, 2013), the development of a huge and arid continental interior and a lowpoint in terrestrial runoff (as suggested by the $^{87}Sr/^{86}Sr$ curve). Thus, the heavy Capitanian $\delta^{13}C$ values could be a response to a marked decline in the weathering of carbonates in Pangea, leading to globally lower carbonate burial rates, and thus forcing a higher f_{org} (i.e. fractional burial of organic matter) and $\delta^{13}C$ without requiring a rise in organic C burial rates.

We test whether the Capitanian nadir in $^{87}Sr/^{86}Sr$ is compatible with the size of the Kamura C isotope excursion by adding a simple strontium cycle to the model of Shields and Mills (2017) (see SI for details). We run the model under its standard present-day configuration, but modify the mafic fraction of total continental weathering and the C isotope composition of the crustal carbonate reservoir in order to replicate Middle Permian $^{87}Sr/^{86}Sr$ and $\delta^{13}C$ values at model initialization (further details in SI). Beginning from steady state, we then impose a 4 Myr period of low erosion rates in the model, reducing the integrated global erosion rate to 25 % of the present-day value, in line with estimates for the Permian (Hay et al., 2006). This reduction in erosion rates results in a nadir in modelled $^{87}Sr/^{86}Sr$ of similar magnitude to the geological record (Fig. 10) and a related positive excursion in modelled carbonate and organic $\delta^{13}C$ of around 2.5 ‰, which is consistent with the magnitude of the Kamura Event. Reduced silicate weathering and carbonate sequestration lead to a contemporary global temperature increase of around 2 °C in

the model. This warming trend during the early-middle Capitanian is similar to that inferred from conodont oxygen isotopes (~3 °C, Chen et al., 2011). We thus propose that the above 'dry continent' scenario, rather than a cooling event, is most consistent with the global nature of the Kamura $\delta^{13}C$ excursion, the accompanying reduction in $^{87}Sr/^{86}Sr$, and the lack of evidence for high rates of C_{org} burial. The model assumes that the isotopic composition of both terrestrial and marine organic carbon is related to the atmosphere-ocean $\delta^{13}C$ value by the same constant offset. This does not prevent the model from assessing global underlying drivers for long-term $\delta^{13}C$ trends, but it means the model cannot incorporate more intricate relationships such as organic matter source mixing or environmentally-driven changes to biological fractionation factors.

5.4 Late Capitanian negative $\delta^{13}C_{org}$ excursion and its causes

In view of the highly variable magnitudes and duration of these negative isotope excursions, proposed causes for the global negative (carbonate and organic) C-isotope shift include: release of light carbon from volcanogenic sources (e.g., Grard et al., 2005); release of methane from gas hydrates (e.g., Krull and Retallack, 2000); erosion of organic matter during regression (e.g., Kump and Arthur, 1999), the collapse of primary productivity (e.g., Kump and Arthur, 1999); upwelling of isotopically light, euxinic waters into shallow water levels due to the oceanic overturn (e.g., Kump et al., 2005). It is possible to evaluate at least some of these possibilities for the Capitanian excursion.

Volcanic and methane hydrate sources: The ELIP eruption has long been proposed as the most important cause for this excursion (e.g., Wignall et al. 2009). Tuffs (dated to 261.6 ± 1.6 Ma) appear in the uppermost Gufeng Formation around the same time as the eruptions (*J. altudaensis* zone to *J. xuanhanensis* zone), and are likely sourced by the Emeishan Province

(Zhang et al., 2019). Mantle carbon has light isotopic composition (-6 ‰, Saunders, 2005), but the ELIP is a relatively small province (< 0.5 million km^3 of extrusives) and so is unlikely to have contributed substantially to the negative excursion. Also, it is difficult to maintain low carbon isotopic values in the ocean-atmosphere system for such long duration of the $\delta^{13}C$ excursion at many sections (Jost et al., 2014). They further argue against the prominent effect of Emeishan outgasing on changes of carbon isotope based on the evidence of carbon and calcium cycle in the shallow marine carbonate. This limited effect could also be supported by the small fluctuation of $\delta^{13}C_{org}$ in the deep-water sediments (e.g., Nishikane et al., 2014), which could be more strongly influenced by atmospheric CO_2 changes (Takahashi et al., 2010). Contact metamorphism may have generated significant carbon release from the environs of the Emeishen Province (Retallack and Jahren, 2008), but the subcrop is dominated by Palaeozoic carbonates which are isotopically heavy (Ganino and Arndt, 2009). Methane release is a popular mechanism used to explain sharp, negative $\delta^{13}C$ excursions but Bond et al. (2010b) have argued that, for the Capitanian example, the rate of decrease was two orders of magnitude slower than seen for other, more plausible, examples of this phenomenon (e.g., Katz et al., 1999). Thus, the small and slow negative $\delta^{13}C_{org}$ excursion (N5, ~1-2 ‰) developed over a relatively long time interval (~1 Ma) in our studied sections (Fig. 8) is difficult to explain by a dissociation of methane hydrates.

Productivity collapse: Upwelling-related high productivity declined on the northern margin of the South China continent before the late Capitanian (Zhang et al. 2018). However, the abrupt decrease of primary productivity was slightly later than the beginning of this negative carbon isotope excursion (Fig. 4). A similar scenario found by Wei et al. (2017) in the Middle Yangtze region also argued against this cause. In addition, the stepwise biotic decline during the

Capitanian would also not be anticipated to lead to a rapid negative carbon isotopic excursion.

Anoxic excursion into shallow waters: Saitoh et al. (2013) suggested that the negative excursion can be explained by the local incursion of intermediate to deep anoxic waters with isotopically light carbon isotope in the Upper Yangtze region. However, such anoxic conditions as indicated by increased TS/TOC ratios (> 0.36, Fig. 4), which plot above the "normal marine line" (Fig. S2), persisted on the northern margin of South China throughout the Capitanian suggesting this is an unlikely cause. Notably, the appearance and enhancement of this anoxic condition in PDS section are much later than the negative $\delta^{13}C_{org}$ shifts and further preclude this explanation. Importantly, local upwelling solely restricted in the eastern margin of the Palaeo-Tethys cannot explain the global nature of this negative C isotope excursion. Additionally, the inconsistent negative excursion between redox proxies and $\delta^{13}C$ in many sections also argue against a causal relationship between anoxia and carbon isotope shift (e.g., Yan et al., 2013; Kwon et al., 2018).

Regression: A major sequence boundary occurs around the base of the *Jinogondolella xuanhanensis* Zone (Bond et al., 2010a, b; Zhang et al., 2019), and is contemporary with the world-wide negative excursions (Fig. 8) suggesting it is likely to be a controlling factor (Lai et al., 2008; Wei et al., 2017). Re-oxidized organic matter due to the sea level fall could have release abundant ^{13}C-depleted carbon from exposed continental shelves into seawater, which could eventually lead to the decreased magnitudes of negative excursion from continental margin settings to the deep-water environments (Takahashi et al., 2010). This can be testified by the increasing magnitude of the excursion from deep to shallow-water areas in both $\delta^{13}C_{carb}$ and $\delta^{13}C_{org}$ records (Fig. 11). The relatively slow negative shift of $\delta^{13}C_{org}$ further suggest that the intrabasin variability in the Lower Yangtze region could be resulted from the increased input of

isotopically-light carbon sourced from the terrestrial decomposition of organic matter due to the sea level drop.

6. Conclusion

The $^{13}C_{org}$ records at three Middle Permian chert-mudstone sections were obtained from the Low Yangtze region and used to construct a chemostratigraphic framework in combination with published ^{13}C curves. Source of organic matter and diagenetic changes played a limited role in affecting the $\delta^{13}C_{org}$ values, thus indicating an effective and original Middle Permian $\delta^{13}C$ signal. The $\delta^{13}C_{org}$ records increased from late Kungurian to early Guadalupian and then decreased to the late Wordian/early Capitanian. Early-mid Capitanian was characterized by elevated $\delta^{13}C_{org}$ values but then followed by a negative excursion with variable magnitude during the middle-late Capitanian. In combination with the well-established radiolarian zones and precise radio-isotopic ages of boundary tuffs, this continuously high-resolution $\delta^{13}C_{org}$ chemostratigraphic correlation scheme could be used as an alternative approach to date or establish correlation with the well-dated events.

The early-middle Capitanian high positive $\delta^{13}C_{org}$ excursion is recorded locally in organic-rich sediments (high TOC contents), indicating that high productivity in the region may have been driven by intensified upwelling. However, the 'Kamura Event' does not appear to be a global productivity event, and box modelling indicates that the coupled $\delta^{13}C$-$^{87}Sr/^{86}Sr$ records may be better explained by a global reduction in erosion and carbonate weathering rates, driven by the peak development of an arid continental interior on Pangaea. A negative $\delta^{13}C_{org}$ excursion correlated with the Captianian mass extinction may be mainly caused by input of isotopically-light carbon sourced from the terrestrial decomposition of organic matter during

regression.

Acknowledgements

We thank Chang Xu for providing constructive suggestions. This work was supported by the National Natural Science Foundation of China (Grant nos. 41772128, 41372127, U1663202, 41690131 and 41802175) and the program B for Outstanding PhD candidate of Nanjing University. Paul B. Wignall was funded by Natural Environment Research Council (NERC) grant (NE/P0137224/1), part of the Biosphere Evolution, Transitions and Resilience (BETR) programme. We acknowledge Haijun Song and an anonymous reviewer for their comments that substantially improved this work, as well as Prof. Andrea Festa for editorial handling.

References

Arthur, M.A., Dean, W.E., Claypool, G.E., 1985. Anomalous ^{13}C enrichment in modern marine organic carbon. Nature 315, 216–218.

Bagherpour, B., Bucher, H., Schneebeli-Hermann, E., Vennemann, T., Chiaradia, M., Shen, S., 2018. Early late Permian coupled carbon and strontium isotope chemostratigraphy from South China: extended Emeishan volcanism? Gondwana Research 58, 58–70.

Berner, R.A., Raiswell, R., 1984. C/S method for distinguishing fresh-water from marine sedimentary-rocks. Geology 12 (6), 365–368.

Birgenheier, L.P., Frank, T.D., Fielding, C.R., Rygel, M.C., 2010. Coupled carbon isotopic and sedimentological records from the Permian system of eastern Australia reveal the response of atmospheric carbon dioxide to glacial growth and decay during the late Palaeozoic Ice Age. Palaeogeography, Palaeoclimatology, Palaeoecology 286, 178–193.

Bond, D.P.G., Hilton, J., Wignall, P.B., Ali, J.R., Stevens, L.G., Sun, Y., Lai, X., 2010a. The Middle Permian (Capitanian) mass extinction on land and in the oceans. Earth-Science Reviews 102, 100–116.

Bond, D.P.G., Wignall, P.B., Wang, W., Izon, G., Jiang, H.S., Lai, X.L., Sun, Y.D., Newton, R.J., Shao, L.Y., Vedrine, S., Cope, H., 2010b. The mid-Capitanian (Middle Permian) mass extinction and carbon isotope record of South China. Palaeogeography Palaeoclimatology Palaeoecology 292, 282–294.

Bond, D.P.G., Wignall, P.B., Joachimski, M.M., Sun, Y., Savov, I., Grasby, S.E., Beauchamp, B., Blomeier, D.P.G., 2015. An abrupt extinction in the Middle Permian (Capitanian) of the Boreal Realm (Spitsbergen) and its link to anoxia and acidification. Geological Society of America Bulletin 127, 1411–1421.

Buggisch, W., Wang, X., Alekseev, A.S., Joachimski, M.M., 2011. Carboniferous–Permian carbon isotope stratigraphy of successions from China (Yangtze platform), USA (Kansas) and Russia (Moscow Basin and Urals). Palaeogeography, Palaeoclimatology, Palaeoecology 301, 18–38.

Bureau of Geology and Mineral Resources of Anhui Province. 1989. Stratigtaphic record of Anhui Province. Anhui Science and Technology Publishing House. (in Chinese)

Cao, C., Cui, C., Chen, J., Summons, R. E., Shen, S., Zhang, H., 2018. A positive C-isotope excursion induced by sea-level fall in the middle Capitanian of South China. Palaeogeography, Palaeoclimatology, Palaeoecology 505, 305–316. https://doi.org/10.1016/j.palaeo.2018.06.010

Chen, B., Joachimski, M. M., Sun, Y., Shen, S., Lai, X., 2011. Carbon and conodont apatite oxygen isotope records of Guadalupian–Lopingian boundary sections: Climatic or sea-level signal? Palaeogeography, Palaeoclimatology, Palaeoecology 311, 145–153. https://doi.org/10.1016/j.palaeo.2011.08.016

Cheng, C., Li, S., Xie, X., Cao, T., Manger, W., Busbey, A., 2019.Permian carbon isotope and clay mineral records from the Xikou section, Zhen'an, Shaanxi Province, central China: Climatological implications for the easternmost Paleo-Tethys. Palaeogeography, Palaeoclimatology, Palaeoecology 514, 417–422

Des Marais, D.J.,Strauss, H.,Summons,R.E., Hayes, J.M., 1992. Carbon isotope evidence for the stepwise oxidation of the Proterozoic environment. Nature 359, 605–609.

Ernst, R.E., 2014. Large Igneous Provinces. Cambridge University Press, pp. 653.

Ganino, C., Arndt, N. T., 2009. Climate changes caused by degassing of sediments during the emplacement of large igneous provinces. Geology 37, 323–326.

Gradstein, F.M., Ogg, J.G., Schmitz, M.D., Ogg, G.M. (eds.) 2012. The Geologic Time Scale. Vol. 1. Elsevier, Boston.

Grard, A., Francois, L. M., Dessert, C., Dupré, B., Godderis, Y., 2005. Basaltic volcanism and mass extinction at the Permo-Triassic boundary: environmental impact and modeling of the global carbon cycle. Earth and Planetary Science Letters 234, 207–221.

Grasby, S. E. , Beauchamp, B., 2008. Intrabasin variability of the carbon-isotope record across the Permian–Triassic transition, Sverdrup basin, arctic Canada. Chemical Geology 253(3-4), 0–150.

Grasby, S. E. , Benoit, B. , Bond, D. P. G. , Wignall, P. B. , Hamed, S., 2016. Mercury anomalies associated with three extinction events (Capitanian crisis, Latest Permian extinction and the Smithian/Spathian extinction) in NW Pangea. Geological Magazine 153, 13.

Hay, W., Migdisov, A., Balukhovsky, A., Wold, C., Flögel S., Söding, E. 2006. Evaporites and the salinity of the ocean during the phanerozoic: implications for climate, ocean circulation and life. Palaeogeography Palaeoclimatology Palaeoecology, 240, 3–46.

Hayes, J.M., Popp, B.N., Takigiku, R., Johnson, M., 1989. An isotopic study of biogeochemical relationships between carbonates and organic carbon in the Greenhorn Formation. Geochimica et Cosmochimica Acta 53, 2961–2972.

Hayes, J.M., Strauss, H., Kaufman, A.J., 1999. The abundance of ^{13}C in marine organic matter and isotopic fractionation in the global biogeochemical cycle of carbon during the past 800 Ma. Chemical Geology 161, 103–125.

Hermann, E., Hochuli, P.A., Bucher, H., Vigran, J.O., Weissert, H., Bernasconi, S.M., 2010. A close-up view on the Permian–Triassic boundary based on extended organic carbon isotope records from Norway (Trøndelag and Finnmark Platform). Global and Planetary Change 74, 156-167.

Isozaki, Y., Kawahata, H., Ota, A. 2007a. A unique carbon isotope record across the Guadalupian-Lopingian (Middle-Upper Permian) boundary in mid-oceanic paleo-atoll carbonates: The high-productivity "Kamura event" and its collapse in Panthalassa. Global and Planetary Change 55, 21–38.

Isozaki, Y., Kawahata, H., Minoshima, K., 2007b. The Capitanian (Permian) Kamura cooling event: the beginning of the Paleozoic–Mesozoic transition. Palaeoworld 16, 16–30.

Isozaki, Y., Aljinovic, D., Kawahata, H., 2011. The Guadalupian (Permian) Kamura event in European Tethys. Palaeogeography Palaeoclimatology Palaeoecology 308, 12–21.

Jin, Y., Zhang, J., Shang, Q., 1994. Two Phases of the End-Permian Mass Extinction. Canadian Society of Petroleum Geologists Memoir 17, 813–822.

Jost, A. B., Mundil, R., He, B., Brown, S. T., Altiner, D., Sun, Y., Donald, J. D., Payne, J. L., 2014. Constraining the cause of the end-Guadalupian extinction with coupled records of carbon and calcium isotopes. Earth and Planetary Science Letters 396, 201–212. https://doi.org/10.1016/j.epsl.2014.04.014

Kametaka, M., Nagai, H., Zhu, S., Takebe, M., 2009. Middle Permian radiolarians from Anmenkou, Chaohu, Northeastern Yangtze platform, China. Island Arc 18, 108–125.

Kametaka, M., Takebe, M., Nagai, H., Zhu, S., Takayanagi, Y., 2005. Sedimentary environments of the Middle Permian phosphorite-chert complex from the northeastern Yangtze platform, China; the Gufeng Formation: a continental shelf radiolarian chert. Sedimentary Geology, 174, 197–222. https://doi.org/10.1016/j.sedgeo.2004.12.005

Katz, M.E., Pak, D.K., Dickens, G.R., Miller, K.G., 1999. The source and fate of massive carbon input during the latest Paleocene thermal maximum. Science 286, 1531–1533.

Korte, C., Jasper, T., Kozur, H.W. and Veizer, J., 2005. $\delta^{18}O$ and $\delta^{13}C$ of Permian brachiopods: A record of seawater evolution and continental glaciation. Palaeogeography, Palaeoclimatology, Palaeoecology 224, 333–351.

Krull, E.S., Retallack, G.J., 2000. $\delta^{13}C$ depth profiles from paleosols across the Permian–Triassic boundary: evidence for methane release. Geological Society of America Bulletin 112, 1459–1472

Ruhl, M., Kürschner, W.M., Krystyn, L., 2009. Triassic–Jurassic organic carbon isotope stratigraphy of key sections in the western Tethys realm (Austria). Earth and Planetary Science Letters 281, 169–187. http://dx.doi.org/10.1016/j.epsl.2009.02.020.

Kump, L.R., Arthur, M.A., 1999. Interpreting carbon-isotope excursions: carbonates and organic matter. Chemical Geology 161, 181–198.

Kump, L.R., Pavlov, A., Arthur, M.A., 2005. Massive release of hydrogen sulfide to the surface ocean and atmosphere during intervals of oceanic anoxia. Geology 33, 397–400.

Kwon, H., Kim, M., Lee, Y., 2018. Mercury evidence from the Sino-Korean block for Emeishan volcanism during the Capitanian mass extinction. Geological Magazine, 1–6.

Lai, X., Wang, W., Wignall, P.B., Bond, D.P.G., Jiang, H., Ali, J.R., John, E.H., Sun, Y., 2008. Palaeoenvironmental change during the end-Guadalupian (Permian) mass extinction in Sichuan, China. Palaeogeography Palaeoclimatology Palaeoecology 269, 78–93.

Laya, J. C. , Tucker, M. E. , Cke, D. R. G., Perez-Huerta, A., 2013. Carbon, oxygen and strontium isotopic composition of low-latitude Permian carbonates (Venezuelan Andes): climate proxies of tropical Pangea. Geological Society, London, Special Publications 376, 367–385

Liang D., Guo, T., Bian, L., Chen, J., Zhao, Z., 2009. Some progresses on studies of hydrocarbon generation and accumulation in marine sedimentary regions, Southern China (Part 3): controlling factors on the sedimentary facies and development of Palaeozoic marine source rocks. Marine origin petroleum geology 14, 1–19 (in Chinese, with English Abstr.).

Liu, C. , Du, Y. , Jarochowska, E. , Yan, J. , Munnecke, A. , Lu, G., 2018. A major anomaly in the carbon cycle during the late Cisuralian (Permian): timing, underlying triggers and implications. Palaeogeography, Palaeoclimatology, Palaeoecology 491, 112–122

Luo, G., Algeo, T. J., Huang, J., Zhou, W., Wang, Y., Yang, H., Richoz, S., Xie, S., 2014. Vertical $\delta^{13}C_{org}$ gradients record changes in planktonic microbial community composition during the end-Permian mass extinction. Palaeogeography, Palaeoclimatology, Palaeoecology 396, 119–131. https://doi.org/10.1016/j.palaeo.2014.01.006

McArthur, J.M., Howarth, R.J., Shields, G.A., 2012. Strontium Isotope Stratigraphy, the Geologic Time Scale. Elsevier, Boston, pp. 127–144.

Meyers, P.A., 1997. Organic geochemical proxies of paleoceanographic, paleolimnologic, and paleoclimatic

processes. Organic Geochemistry 27, 213–250

Montañez, I.P., Tabor, N.J., Niemeier, D., DiMichele, W.A., Frank, T.D., Fielding, C.R., Isbell, J.L., Birgenheier, L.T., Rygel, M., 2007. CO_2-forced climate and vegetation instability during Late Paleozoic glaciation. Science 315, 87–91.

Nishikane, Y., Kaiho, K., Henderson, C. M., Takahashi, S., Suzuki, N., 2014. Guadalupian–Lopingian conodont and carbon isotope stratigraphies of a deep chert sequence in Japan. Palaeogeography, Palaeoclimatology, Palaeoecology 403, 16–29. https://doi.org/10.1016/j.palaeo.2014.02.033

Retallack, G. J., Jahren, A. H., 2008. Methane release from igneous intrusion of coal during Late Permian extinction events. The Journal of Geology, 116, 1–20. https://doi.org/10.1086/524120

Saitoh, M., Isozaki, Y., Ueno, Y., Yoshida, N., Yao, J., Ji, Z., 2013. Middle-Upper Permian carbon isotope stratigraphy at Chaotian, South China: Pre-extinction multiple upwelling of oxygen-depleted water onto continental shelf. *Journal of Asian Earth Sciences*, 67-68, 51–62.

Saunders, A. D., 2005. Large igneous provinces: origin and environmental consequences. Elements 1, 259–263.

Shen, S. Z., Cao, C. Q., Zhang, H., Bowring, S. A., Henderson, C. M., Payne, J. L., Davydov, V.I., Chen, B., Yuan, D., Zhang Y., Wang, W., Zheng, Q., 2013. High-resolution $\delta^{13}C_{carb}$ chemostratigraphy from latest Guadalupian through earliest Triassic in South China and Iran. Earth and Planetary Science Letters 375, 156–165.

Shi, Z., Yin, G., Li, W., Yang, H., Zhang, J., Lu, L., Tian, Y., Wang, Y., 2017. Major geological events in the late Guadalupian and carbon–strontium isotope responses in the Yangtze platform, South China. Canadian Journal of Earth Sciences 54, 1025–1032. https://doi.org/10.1139/cjes-2017-0103

Shields, G. A., Mills, B. J., 2017. Tectonic controls on the long-term carbon isotope mass balance. Proceedings of the National Academy of Sciences 144, 4318–4323

Strauss, H., Peters-Kottig, W., 2003. The Paleozoic to Mesozoic carbon cycle revisited: the carbon isotopic composition of terrestrial organic matter. Geochemistry, Geophysics, Geosystems 4, 15.

Takahashi, S. , Kaiho, K. , Oba, M. , Kakegawa, T., 2010. A smooth negative shift of organic-carbon isotope ratios at an end-Permian mass extinction horizon in central pelagic Panthalassa. Palaeogeography, Palaeoclimatology, Palaeoecology 292, 532–539

Thomas, B.M., Willink, R.J., Grice, K., Twitchett, R.J., Purcell, R.R., Archbold, N.W., George, A.D., Tye, S., Alexander, R., Foster, C.B., Barber, C.J., 2004. Unique marine Permian-Triassic boundary section from Western Australia. Australian Journal of Earth Sciences 51, 423–430.

Traverse, A., 2007. Paleopalynology, second ed. Springer, Dordrecht, p. 813

Twichell, S.C., Meyers, P.A., Diester-Haass, L., 2002. Significance of high C/N ratios in organic-carbon-rich Neogene sediments under the Benguela Current upwelling system. Organic Geochemistry 33, 715–722.

Tyson, R.V., 1995. Sedimentary Organic Matter: Organic Facies and Palynofacies. Chapman and Hall, London, p. 615.

Wang, D., Ulrich, S., Ling, H-F., Guo, Q-J., Shields-Zhou, G. A., Zhu, M-Y., Yao, S-P., 2015. Marine redox variations and nitrogen cycle of the early Cambrian southern margin of the Yangtze Platform, South China: evidence from nitrogen and organic carbon isotopes. Precambrian Research 267, 209–26.

Wang, J., Jin, Y.G., 2000. Permian palaeogeographic evolution of the Jiangnan Basin, South China. Palaeogeography Palaeoclimatology Palaeoecology 160, 35–44.

Wang, W., Cao, C., Wang, Y., 2004. The carbon isotope excursion on GSSP candidate section of Lopingian-Guadalupian boundary. Earth and Planetary Science Letters 220, 57–67.

Wei, H., Baima, Q., Qiu, Z., Dai, C., 2017. Carbon isotope perturbations and faunal changeovers during the Guadalupian mass extinction in the middle Yangtze Platform, South China. Geological Magazine, 1–17. https://doi.org/10.1017/S0016756817000462

Weissert, H., Joachimski, M., Sarnthein, M., 2008. Chemostratigraphy. Newsl. Stratigr. 42, 145–179.

Wignall, P.B., Sun, Y., Bond, D.P.G., Izon, G., Newton, R.J., Vedrine, S., Widdowson, M., Ali, J.R., Lai, X., Jiang, H., Cope, H., Bottrell, S.H., 2009. Volcanism, mass extinction, and carbon isotope fluctuations in the Middle Permian of China. Science 324, 1179–1182.

Wignall, P.B., Bond, D.P.G., Haas, J., Wang, W., Jiang, H., Lai, X., Altiner, D., Vedrine, S., Hips, K., Zajzon, N., Sun, Y., Newton, R.J., 2012. Capitanian (Middle Permian) mass extinction and recovery in western Tethys: a fossil, facies, and delta C^{13} study from Hungary and Hydra Island (Greece). Palaios 27, 78–89.

Wu, Q., Ramezani, J., Zhang, H., Wang, T.T., Yuan, D.X., Mu, L., Zhang, Y.C., Li, X.H., Shen, S.Z., 2017. Calibrating the Guadalupian Series (Middle Permian) of South China. Palaeogeography, Palaeoclimatology, Palaeoecology 466, 361–372. https://doi.org/10.1016/j.palaeo.2016.11.011

Yan, D., Zhang, L., Qiu, Z., 2013. Carbon and sulfur isotopic fluctuations associated with the end-Guadalupian mass extinction in South China. Gondwana Research 24, 1276–1282. https://doi.org/10.1016/j.gr.2013.02.008

Yin, H., Song, H., 2013. Mass extinction and Pangea integration during the Paleozoic-Mesozoic transition. Science China Earth Sciences 56(11): 1791–1803.

Yao, X., Zhou, Y., Hinnov, L.A., 2015. Astronomical forcing of a Middle Permian chert sequence in Chaohu, South China. Earth and Planetary Science Letters, 422, 206–221.

Zhang, B., Yao, S., Wignall, P. B., Hu, W., Ding, H., Liu, B., Ren, Y., 2018. Widespread coastal upwelling along the Eastern Paleo-Tethys Margin (South China) during the Middle Permian (Guadalupian): Implications for organic matter accumulation. Marine and Petroleum Geology 97, 113–126.

Zhang, B., Yao, S., Wignall, P. B., Hu, W., Liu, B., Ren, Y., 2019. New timing and geochemical constraints on the Capitanian (Middle Permian) extinction and environmental changes in deep-water settings: Evidence from the Lower Yangtze region of South China. Journal of the Geological Society 176, 588–608. https://doi.org/10.1144/jgs2018-137

Zhang, G., Zhang, X., Li, D., Farquhar, J., Shen, S., Chen, X., Shen, Y., 2015. Widespread shoaling of sulfidic waters linked to the end-Guadalupian (Permian) mass extinction. Geology 43, 1091–1094.

Zhou, M., Malpas, J., Song, X., Robinson, P.T., Sun, M., Kennedy, A.K., Lesher, C.M., Keays, R.R., 2002. A temporal link between the Emeishan large igneous province (SW China) and the end-Guadalupian mass extinction. Earth and Planetary Science Letters 196, 113–122.

Fig. captions

Fig. 1 Late Guadalupian palaeogeography of (a) the world (base map from Ron Blakey, http://cpgeosystems.com. (b) South China (modified from Yao et al., 2015) and (c) the Lower Yangtze region. Yellow dots indicate sections of carbon isotope records from other literature. Abbreviations: KS = Kapp Starostin section, FN = Festningen section, PR = Palmar River section, DY = Danyang section, XK = Xikou section, KM = Kamura section, GH = Gujo-hachiman section, SB = Sydney basin, CT = Chaotian section, SS = Shangsi section, DK =Dukou section, TFP = Tianfengping section, RCP = Rencunping section, PDS = Pingdingshan section, GD = Gangdi core, QLS = Qinglongshan section, XJC = Xiongjiachang section, GC= Gouchang section, HC = Houchang section, NQ = Naqing section, GCH = Gongchuan section, PD = Podu section, LSX = Lengshuixi section, TQ = Tieqiao section, PLT = Penglaitan section.

Fig.2 Middle Permian lithologic stratigraphy of the Gufeng and Lower Yinping Formation in the Lower Yangtze region. The geological time and bio-stratigraphy is based on Kametaka et al. (2005, 2009), Yao et al. (2015); Wu et al.(2017), Zhang et al. (2019). Abbreviations: Ser.=Series, Stg.=Stage, F.m.=Formation.

Fig.3 Guadalupian organic carbon isotope changes and correlations of PDS section, GD core and QLS section in the Lower Yangtze region. Abbreviations: Ser.=Series, Stg.=Stage, F.m.=Formation.

Fig. 4 Stratigraphic variations in the PDS section (a), GD core (b) and QLS section (c) for $\delta^{13}C_{org}$, Al, TOC, TN, TS, TS/TOC and TOC/TN ratio. The red dashed line indicates the boundary of Gufeng and

Yinping Formation, and the black dashed line indicates the TS/TOC ratios of modern normal marine sediments (Berner and Raiswell, 1984) and the TOC/TN ratios of modern marine organic matter (Meyers, 1997). The composite geological time is based on Kametaka et al. (2009), Gradstein et al. (2012), Wu et al. (2017) and Zhang et al. (2019). The lithology legend is shown in Fig 3. Abbreviation: F.m. = Formation.

Fig.5 Relative abundance of the major palynofacies components plotted against depth in the PDS section, GD core and QLS section in the Lower Yangtze region. Abbreviations: Ser.=Series, Stg.=Stage, F.m.=Formation.

Fig. 6 Representative photomicrographs of palynofacies components under transmitted white light. Therein, a-g from PDS section, h-l from QLS section, and m-p from GD core. (a-b) Granular AOM from the top Qixia Formation; (c-d) Granular AOM from the Gufeng Formation; (f-g) Elongated, lath-shaped and unstructured woody debris and spores from the lower Yinping Formation; (h) AOM with diffused margins from the top Qixia Formation; (i) Granular AOM from the Gufeng Formation; (j-k) AOM with diffused margins and lath-shaped woody debris; (l) opaque phytoclasts from the lower Yinping Formation; (m) AOM with diffused margins from the top Qixia Formation; (n-o) Granular AOM with angular to sub-angular outlines from the Gufeng Formation; (p) bladed opaque woody debris from the lower Yinping Formation.

Fig. 7 Crossplots of $^{13}C_{org}$ vs TOC, Al, TOC/TN for the (a, b, c) Pingdingshan section, (d, e, f) GD core, (g, h, i) Qinglongshan section.

Fig. 8 Guadalupian $\delta^{13}C_{org}$ chemostratigraphy and global correlation. The $\delta^{13}C_{carb}$ records are from Naqing section (Buggisch et al., 2011), Gou Chang section (Wignall et al., 2009; Bond et al., 2010b), Xiongjiachang section (Wignall et al., 2009; Bond et al., 2010b), Houchang section (Bond et al., 2010b), Rencunping section (Cao et al., 2018), Penglaitan (Wang et al., 2004), Tieqiao section (Yan et al., 2013), Kamura section (Isozaki et al., 2007a, b), Dukou section (Shen et al., 2013), Xikou section (Cheng et al., 2019), Shangsi section (Shen et al., 2013), Podu section (Shi et al., 2017), Lengshuixi section (Shi et al., 2017), and Palmar River section (Laya et al., 2013). The $\delta^{13}C_{org}$ records are from Kapp Starostin section (Bond et al., 2015), Gongchuan section (Liu et al., 2018), Tieqiao section (Yan et al., 2013), Sydney basin (Birgenheier et al., 2010), and Gujo-hachiman section (Nishikane et al., 2014).In the legend, dote indicate $\delta^{13}C_{carb}$ whereas dashed line indicate $\delta^{13}C_{org}$. Abbreviations: Ser.=Series, Stg.=Stage, *P. longl.-P. fus.* = *Pseudoalbaillella longtanensis–P. fusiformis*, *J. Pre-xuan.* = *J. Pre-xuanhanenis*, *C. po.-ho.* = *C. postbitteri hongshuiensis*, *C. po.-po.* = *C. postbitteri postbitteri*. Sections are not to vertical scale.

Fig. 9 Stratigraphic correlation of $\delta^{13}C_{org}$ across the Capitanian interval from Gujo-hachiman section (Nishikane et al., 2014), Pingdingshan section (this study), GD core (this study), Qinglongshan section (this study), Chaotian section (Saitoh et al., 2014), Tianfengping section (Wei et al., 2017); Tieqiao section (Yan et al., 2013), Festningen section (Grasby et al.,2016), Kapp Starostin section (Bond et al., 2015), Sydney basin (Birgenheier et al., 2010), and Danyang section (Kwon et al., 2018), based on biostratigraphic makers, tuff dating age, and proxy of Emeishan volcanism (Hg contents). Sections are not to vertical scale. Yellow band shows the interval of

co-occurrence of volcanism, mass extinction, and carbon isotope negative shift during the middle Capitanian (*J. prexuanhan.-xuanhanensis* zones).

Fig. 10 Model results for the 'dry continent' scenario for the Kamura positive C isotope excursion. Model of Shields and Mills (2017) with strontium cycle added in this work (see SI). (a) Global erosion rate forcing inputted to model. (b) Model global weathering fluxes for carbonates (blue) and organic carbon (red). (c) Model global burial fluxes for carbonates (blue) and organic carbon (red). (d) Model global average surface temperature anomaly. (e) Model $\delta^{13}C$ of new carbonate and organic sediments. (f) Model $^{87}Sr/^{86}Sr$ of seawater, compared to geological record for the Middle Permian (McArthur et al. 2012).

Fig. 11 Plot showing the variability in degree of shift of $\delta^{13}C$ values across the Capitanian mass extinction event. Abbreviations: XJC = Xiongjiachang section, SS = Shangsi section, PD = Podu section, LSX = Lengshuixi section, TQ = Tieqiao section, PLT = Penglaitan section, GH = Gujo-hachiman section, PDS = Pingdingshan section, GD = GD core, QLS = Qinglongshan section, CT = Chaotian section, KP = Kapp Starostin section, DY = Danyang section.

Fig. 1

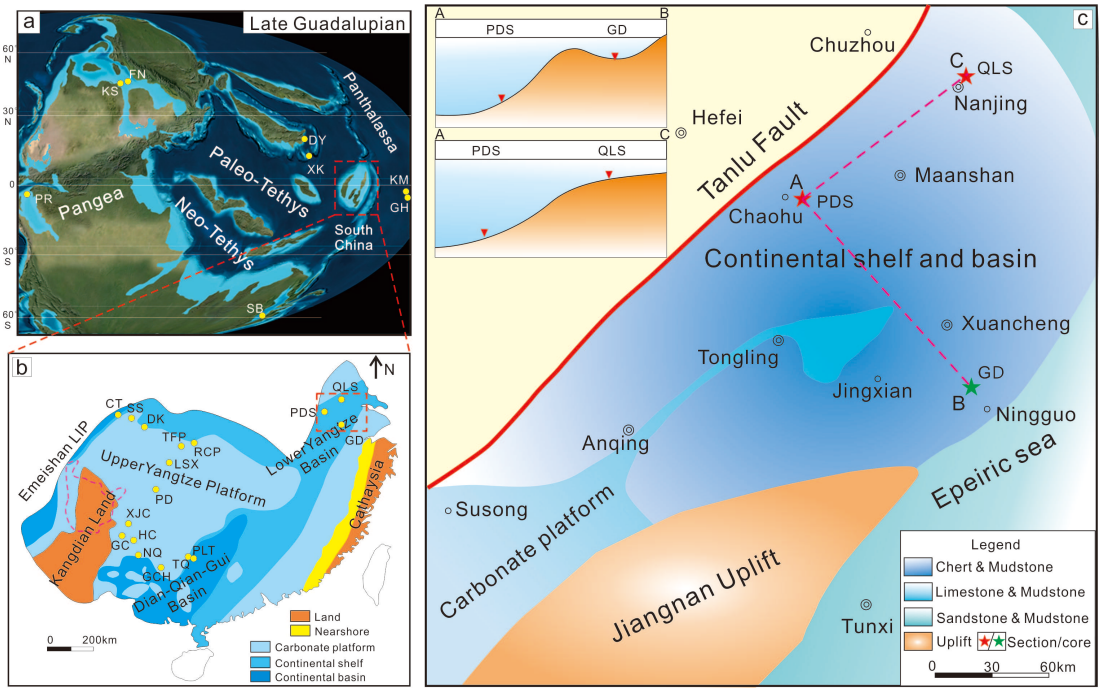
a
Late Guadalupian
60 N
30 N
0
30 S
60 S
FN
KS
DY
XK
KM
GH
PR
SB
Pangea
Paleo-Tethys
Neo-Tethys
Panthalassa
South China
b
N
CT
SS
DK
TFP
RCP
LSX
PD
XJC
HC
GC
NQ
PLT
TQ
GCH
QLS
PDS
GD
Emeishan LIP
Kangdian Land
Upper Yangtze Platform
Lower Yangtze Basin
Cathaysia
Dian-Qian-Gui Basin
0 200km
Land
Nearshore
Carbonate platform
Continental shelf
Continental basin
A
B
PDS
GD
A
C
PDS
QLS
Chuzhou
C
QLS
Nanjing
Hefei
Tanlu Fault
Maanshan
A
PDS
Chaohu
Continental shelf and basin
Xuancheng
Tongling
Jingxian
GD
B
Ningguo
Anqing
Epeiric sea
Susong
Carbonate platform
Jiangnan Uplift
Tunxi
Legend
Chert & Mudstone
Limestone & Mudstone
Sandstone & Mudstone
Uplift
Section/core
0 30 60km

Fig. 2

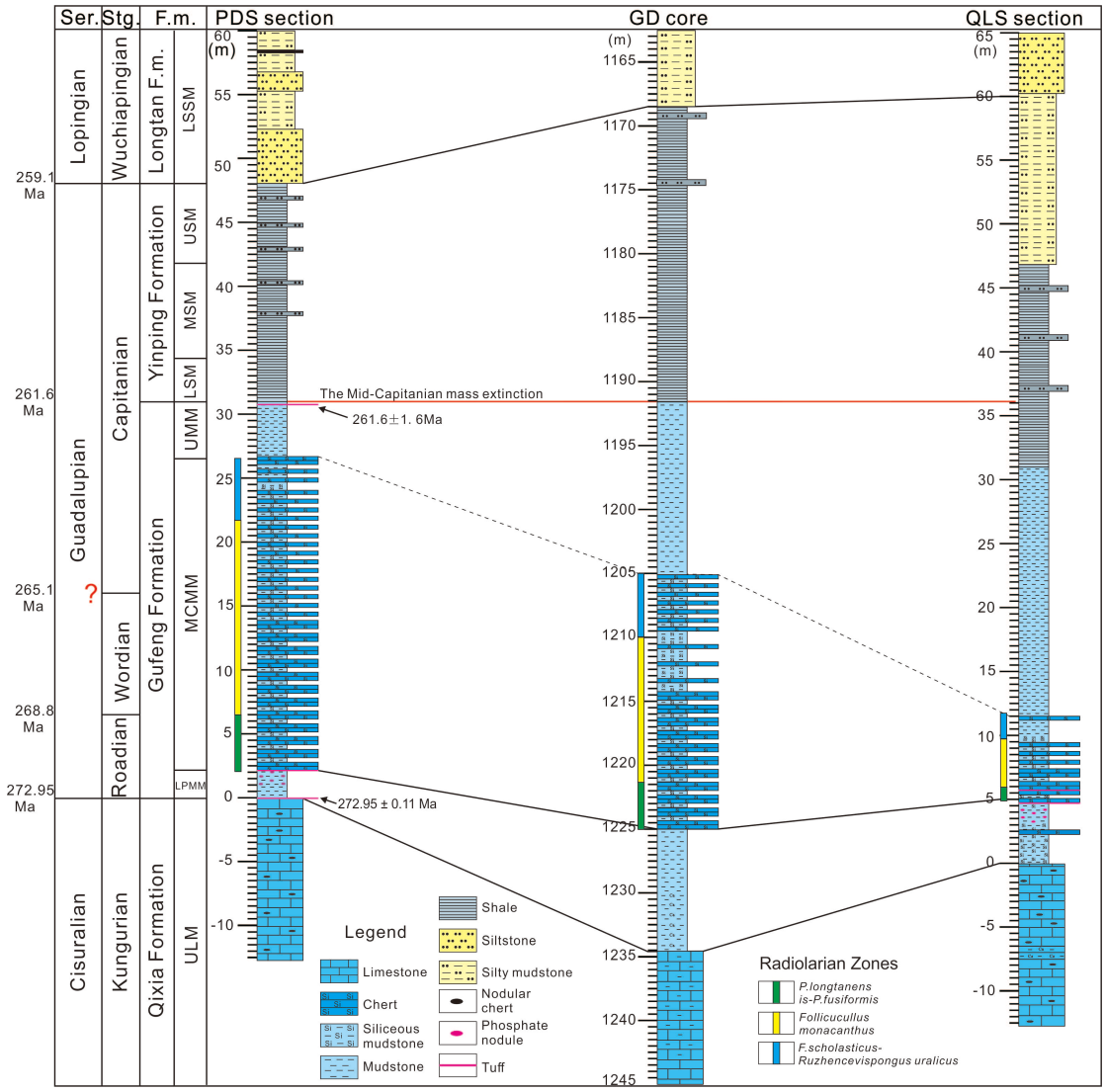
Ser.
Stg.
F.m.
PDS section
GD core
QLS section
Lopingian
Guadalupian
Cisuralian
Wuchiapingian
Capitanian
Wordian
Roadian
Kungurian
Longtan F.m.
Yinping Formation
Gufeng Formation
Qixia Formation
LSSM
USM
MSM
LSM
UMM
MCMM
LPMM
ULM
259.1 Ma
261.6 Ma
265.1 Ma
268.8 Ma
272.95 Ma
?
The Mid-Capitanian mass extinction
261.6±1. 6Ma
272.95 ± 0.11 Ma
Legend
Limestone
Chert
Siliceous mudstone
Mudstone
Shale
Siltstone
Silty mudstone
Nodular chert
Phosphate nodule
Tuff
Radiolarian Zones
P.longtanensis-P.fusiformis
Follicucullus monacanthus
F.scholasticus-Ruzhencevispongus uralicus

Fig. 3

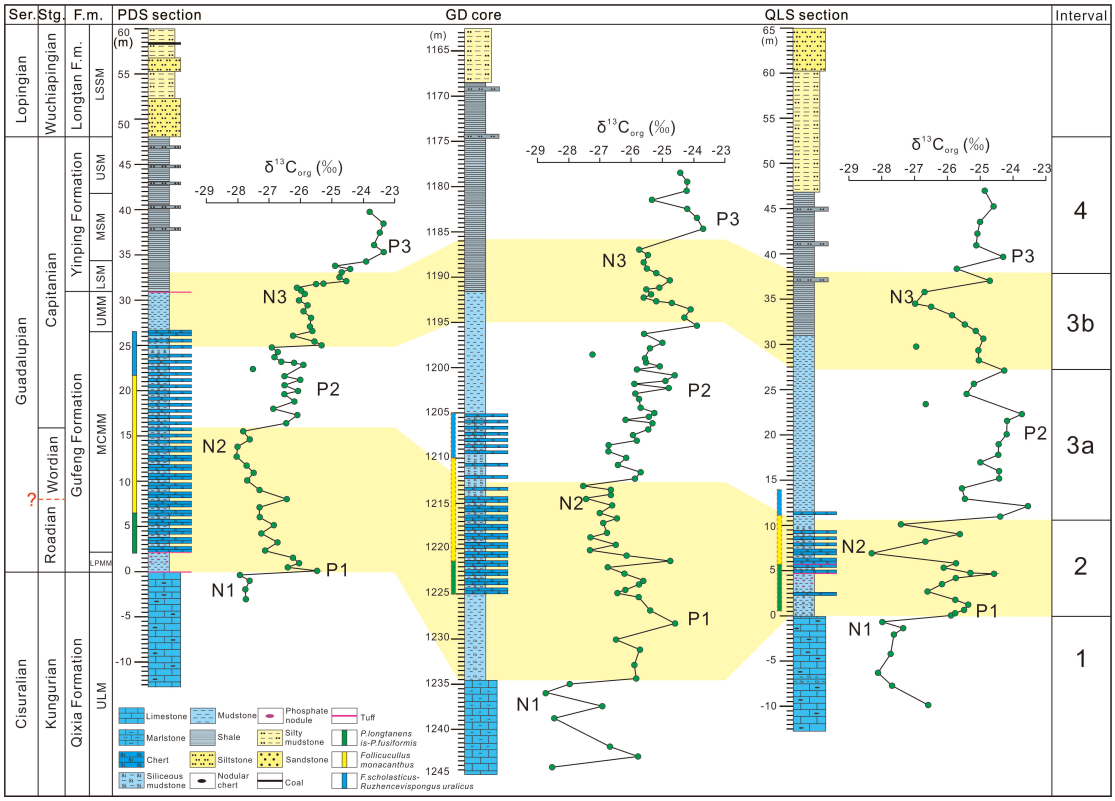
Ser.
Stg.
F.m.
PDS section
GD core
QLS section
Interval
Lopingian
Wuchiapingian
Longtan F.m.
LSSM
Guadalupian
Capitanian
Yinping Formation
USM
MSM
LSM
UMM
Gufeng Formation
MCMM
LPMM
Wordian
Roadian
Cisuralian
Kungurian
Qixia Formation
ULM
δ13Corg (‰)
P1
P2
P3
N1
N2
N3
4
3b
3a
2
1
Limestone
Mudstone
Phosphate nodule
Tuff
Marlstone
Shale
Silty mudstone
P.longtanensis-P.fusiformis
Chert
Siltstone
Sandstone
Follicuculus monacanthus
Siliceous mudstone
Nodular chert
Coal
F.scholasticus-Ruzhencevispongus uralicus

Fig. 4

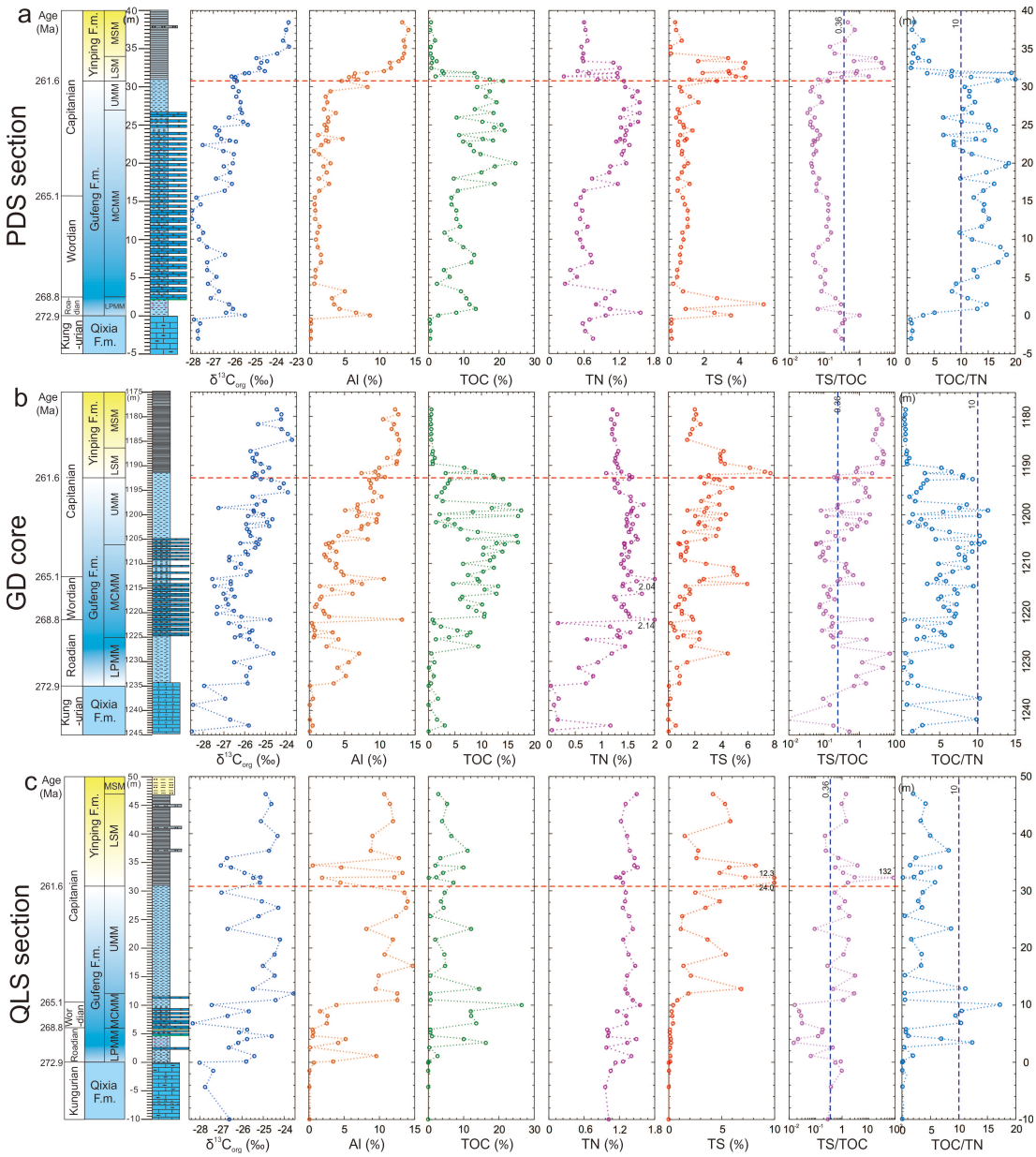
a
PDS section
b
GD core
c
QLS section
Age (Ma)
Yinping F.m.
Gufeng F.m.
Qixia F.m.
Capitanian
Wordian
Roadian
Kungurian
MSM
LSM
UMM
MCMM
LPMM
261.6
265.1
268.8
272.9
(m)
δ13Corg (‰)
Al (%)
TOC (%)
TN (%)
TS (%)
TS/TOC
TOC/TN

Fig. 5

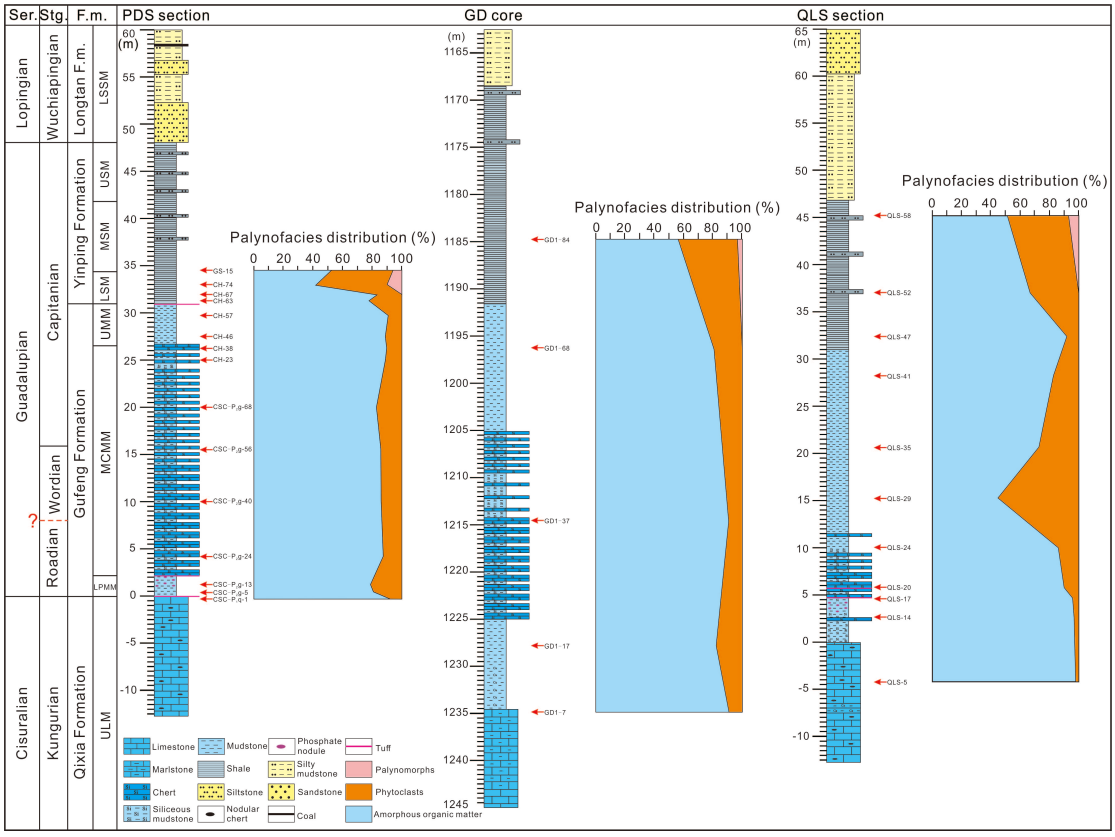
Ser.
Stg.
F.m.
PDS section
GD core
QLS section
Lopingian
Wuchiapingian
Longtan F.m.
LSSM
Guadalupian
Capitanian
Yinping Formation
USM
MSM
LSM
UMM
Gufeng Formation
MCMM
Wordian
Roadian
LPMM
Cisuralian
Kungurian
Qixia Formation
ULM
Palynofacies distribution (%)
0 20 40 60 80 100
Limestone
Mudstone
Phosphate nodule
Tuff
Marlstone
Shale
Silty mudstone
Palynomorphs
Chert
Siltstone
Sandstone
Phytoclasts
Siliceous mudstone
Nodular chert
Coal
Amorphous organic matter

Fig. 6

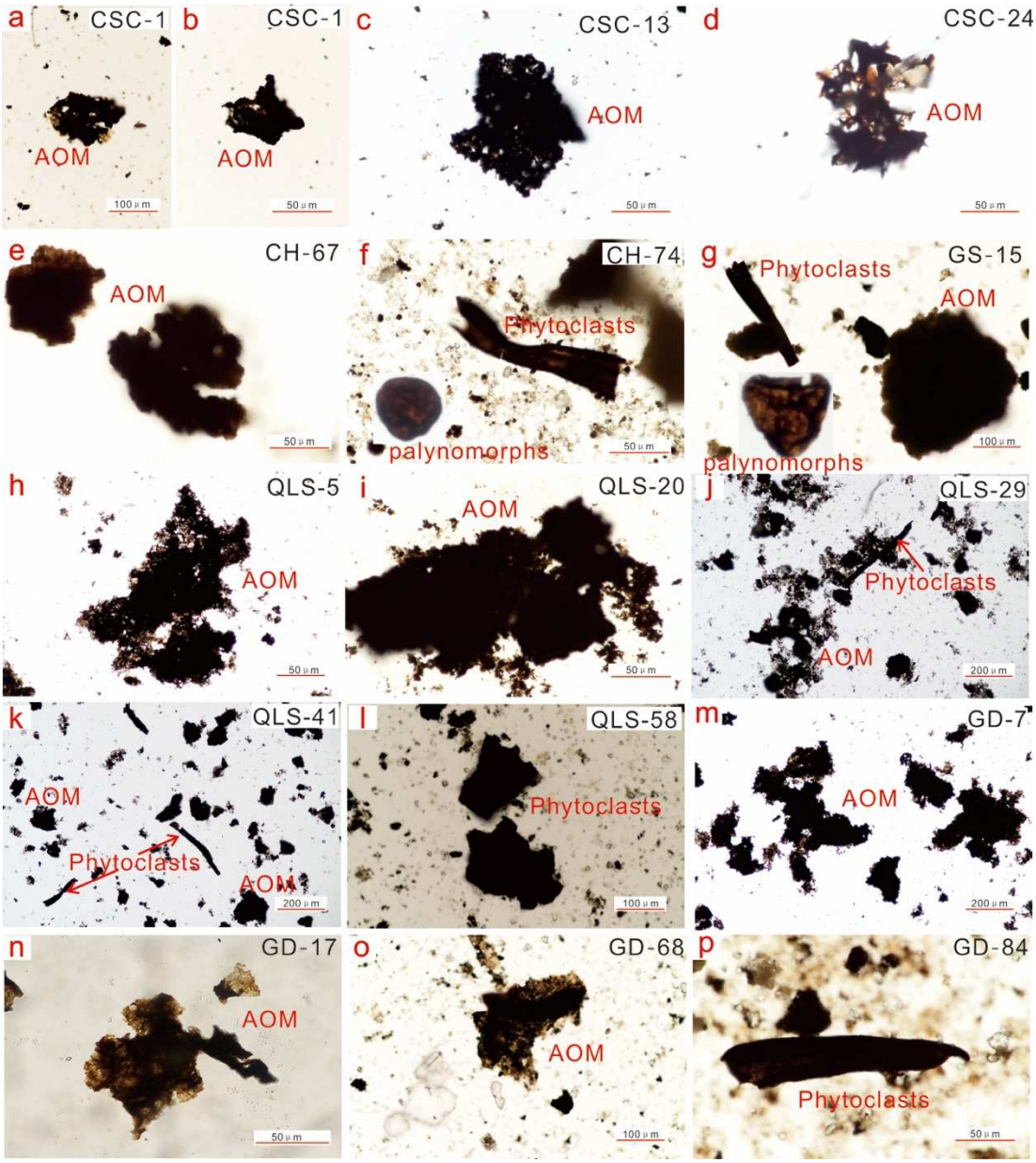
a
CSC-1
AOM
100 μm
b
CSC-1
AOM
50 μm
c
CSC-13
AOM
50 μm
d
CSC-24
AOM
50 μm
e
CH-67
AOM
50 μm
f
CH-74
Phytoclasts
palynomorphs
50 μm
g
GS-15
Phytoclasts
AOM
palynomorphs
100 μm
h
QLS-5
AOM
50 μm
i
QLS-20
AOM
50 μm
j
QLS-29
Phytoclasts
AOM
200 μm
k
QLS-41
AOM
Phytoclasts
AOM
200 μm
l
QLS-58
Phytoclasts
100 μm
m
GD-7
AOM
200 μm
n
GD-17
AOM
50 μm
o
GD-68
AOM
100 μm
p
GD-84
Phytoclasts
50 μm

Fig. 7

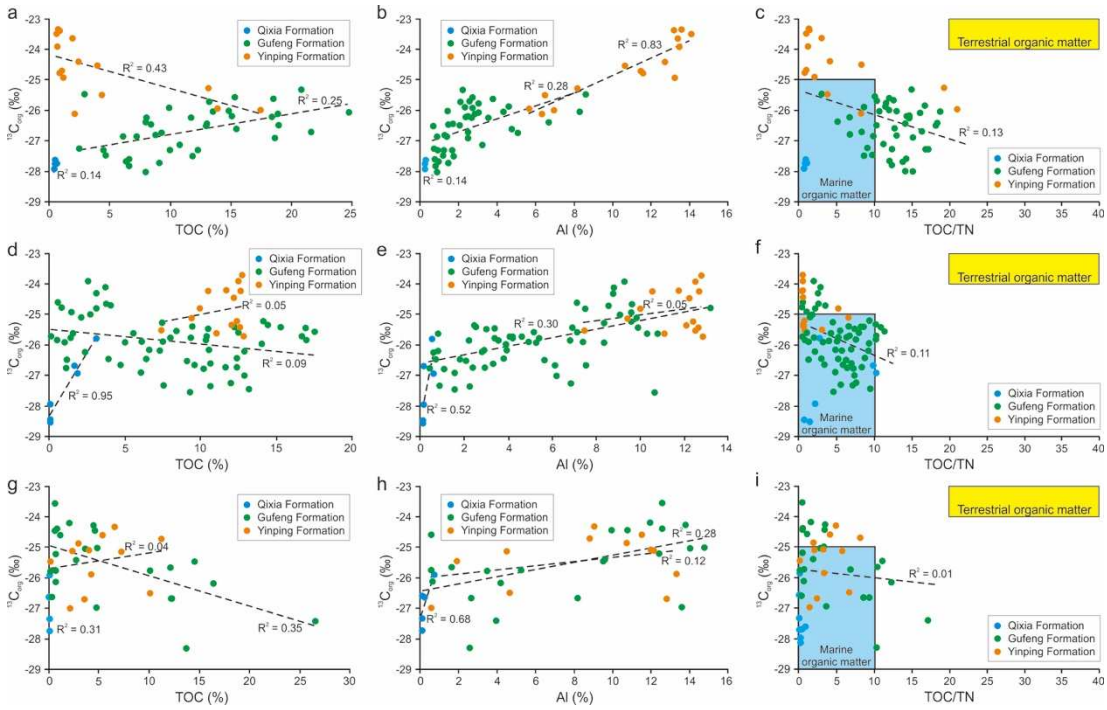
a
b
c
d
e
f
g
h
i
Qixia Formation
Gufeng Formation
Yinping Formation
Terrestrial organic matter
Marine organic matter
TOC (%)
Al (%)
TOC/TN
R² = 0.43
R² = 0.25
R² = 0.14
R² = 0.83
R² = 0.28
R² = 0.14
R² = 0.13
R² = 0.05
R² = 0.09
R² = 0.95
R² = 0.30
R² = 0.05
R² = 0.52
R² = 0.11
R² = 0.04
R² = 0.31
R² = 0.35
R² = 0.28
R² = 0.12
R² = 0.68
R² = 0.01

Fig. 8

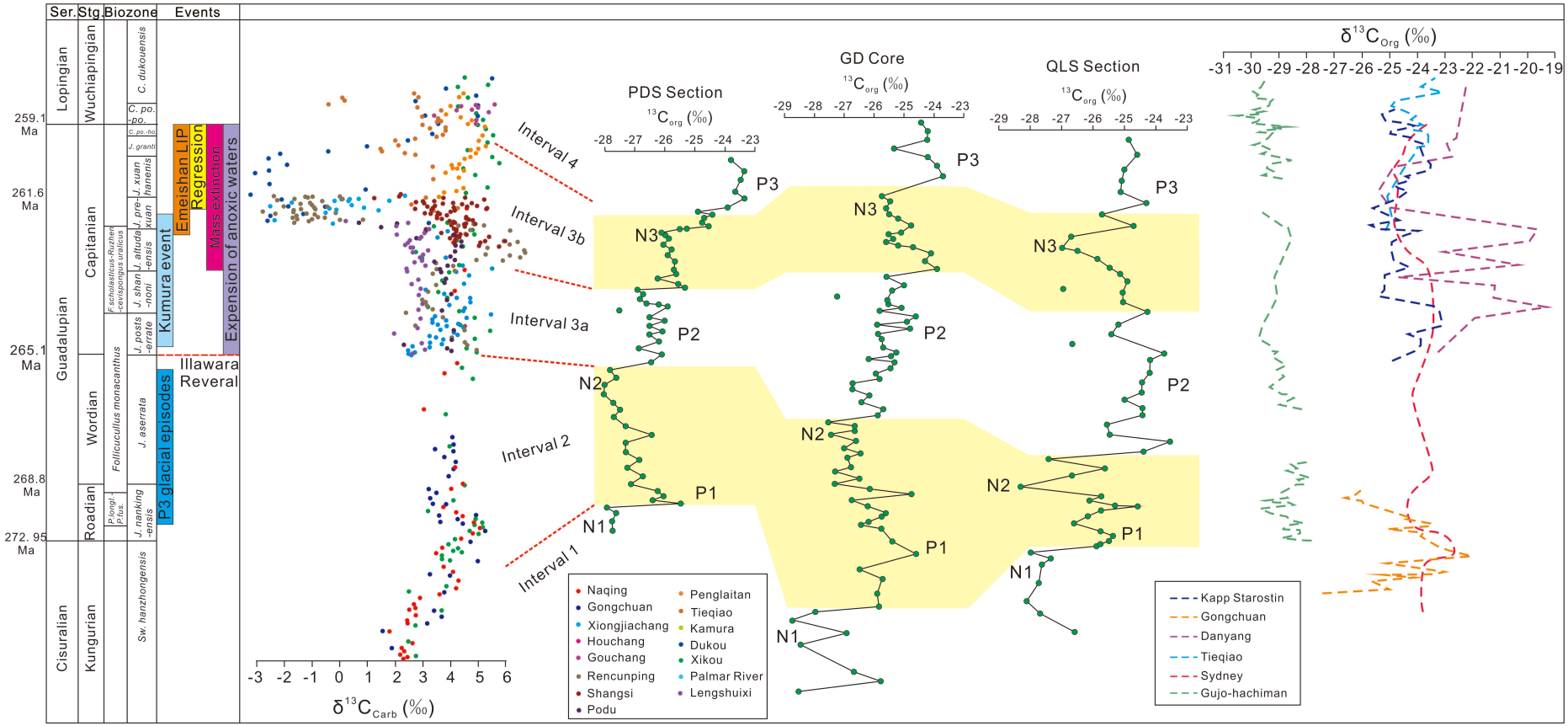
Ser.
Stg.
Biozone
Events
Lopingian
Wuchiapingian
Guadalupian
Capitanian
Wordian
Roadian
Cisuralian
Kungurian
259.1 Ma
261.6 Ma
265.1 Ma
268.8 Ma
272. 95 Ma
C. dukouensis
C. po.-po.
C. po.-ho
J. grantl
J. xuan hanensis
J. pre-xuan
J. altuda-ensis
J. shan-nonl
J. posts-errate
J. aserrata
J. nanking-ensis
Sw. hanzhongensis
Kumura event
Emeishan LIP
Regression
Mass extinction
Expension of anoxic waters
Illawara Reveral
P3 glacial episodes
Interval 4
Interval 3b
Interval 3a
Interval 2
Interval 1
PDS Section
GD Core
QLS Section
P3
N3
P2
N2
P1
N1
δ13Carb (‰)
δ13Corg (‰)
Naqing
Gongchuan
Xiongjiachang
Houchang
Gouchang
Rencunping
Shangsi
Podu
Penglaitan
Tieqiao
Kamura
Dukou
Xikou
Palmar River
Lengshuixi
Kapp Starostin
Gongchuan
Danyang
Tieqiao
Sydney
Gujo-hachiman

Fig. 9

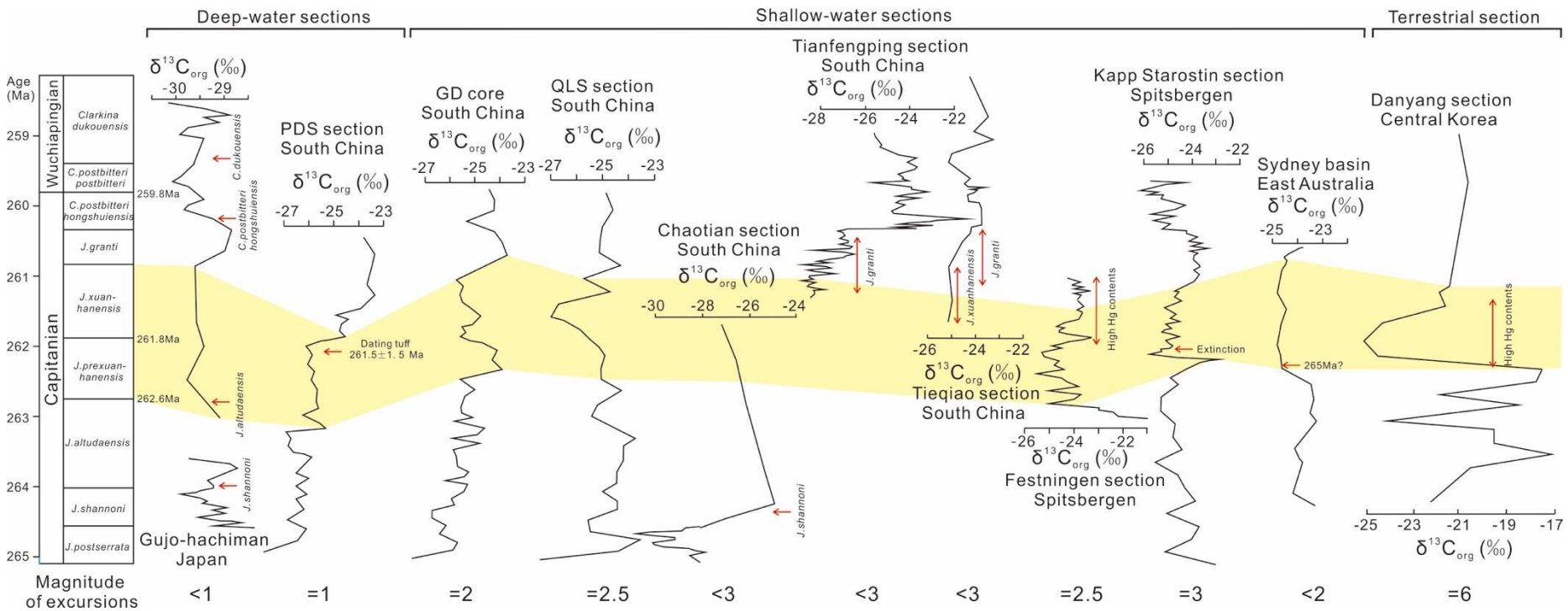
Deep-water sections
Shallow-water sections
Terrestrial section
Age (Ma)
Wuchiapingian
Capitanian
Clarkina dukouensis
C.postbitteri postbitteri
C.postbitteri hongshuiensis
J.granti
J.xuan-hanensis
J.prexuan-hanensis
J.altudaensis
J.shannoni
J.postserrata
259.8Ma
261.8Ma
262.6Ma
Gujo-hachiman Japan
PDS section South China
Dating tuff 261.5±1. 5 Ma
GD core South China
QLS section South China
Chaotian section South China
Tianfengping section South China
Tieqiao section South China
Festningen section Spitsbergen
Kapp Starostin section Spitsbergen
Sydney basin East Australia
Danyang section Central Korea
High Hg contents
Extinction
265Ma?
Magnitude of excursions
<1
=1
=2
=2.5
<3
<3
<3
=2.5
=3
<2
=6

Fig. 10

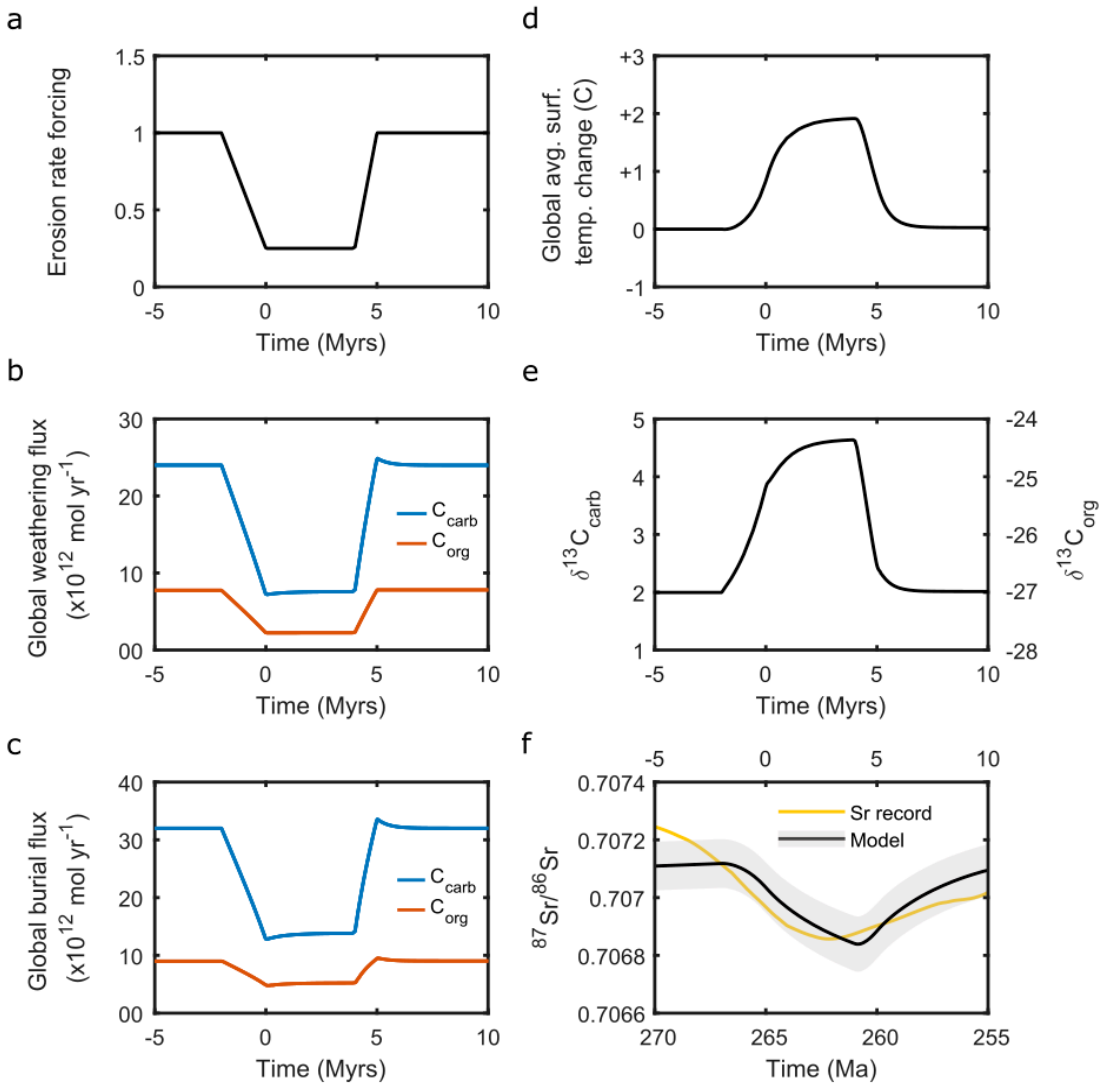
a
Erosion rate forcing
1.5
1
0.5
0
-5
0
5
10
Time (Myrs)
d
Global avg. surf. temp. change (C)
+3
+2
+1
0
-1
-5
0
5
10
Time (Myrs)
b
Global weathering flux (x10^12 mol yr^-1)
30
20
10
00
C carb
C org
-5
0
5
10
Time (Myrs)
e
δ13C carb
δ13C org
5
4
3
2
1
-24
-25
-26
-27
-28
-5
0
5
10
Time (Myrs)
c
Global burial flux (x10^12 mol yr^-1)
40
30
20
10
00
C carb
C org
-5
0
5
10
Time (Myrs)
f
87Sr/86Sr
0.7074
0.7072
0.707
0.7068
0.7066
Sr record
Model
270
265
260
255
Time (Ma)

Fig. 11

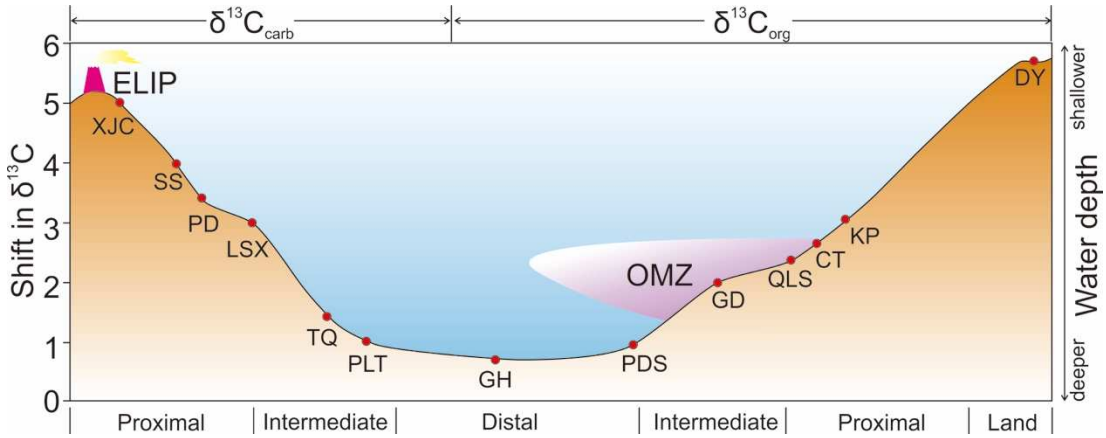
δ13Ccarb
δ13Corg
Shift in δ13C
6
5
4
3
2
1
0
ELIP
XJC
SS
PD
LSX
TQ
PLT
GH
PDS
GD
QLS
CT
KP
DY
OMZ
shallower
Water depth
deeper
Proximal
Intermediate
Distal
Intermediate
Proximal
Land

Supplementary information for:

Middle Permian organic carbon isotope stratigraphy and the origin of the Kamura Event.

Bolin Zhang et al.

1. Supplementary Figure

Fig. S1 shows field pictures of the outcrop and different lithological units of the Qinglongshan (QLS) section.

Fig. S1 Field photographs of the Qinglongshan (QLS) section. (A) Overview of the Permian strata, including Qixia, Gufeng, Yinping and Longtan Formations. The red line indicates their boundary position. (B) A close view of disconformity showing an irregular surface between limestone of the Qixia Formation (P_1q) and mudstone of the Gufeng Formation (P_2g). (C) Close-up view of phosphate nodule-bearing mudstone in the LPMM. (D) Close-up view of chert -siliceous mudstone sequence in the MCMM. (E) A close view of conformity between chert of the MCMM and carbonaceous mudstone of the UMM. (F) Close-up view of black shale in the LSM. (G) Close-up view of yellow sandstone of the lower part of the Longtan Formation.

Fig. S2 shows crossplots for the GD core, QLS section and PDS section. IN the manuscript we argue that the low TOC/TN ratios in all plots are indicative of a primary marine source with minor terrestrial influence. TS/TOC ratios above the 'normal marine line' demonstrate

persistent anoxia on the northern margin of South China throughout the Capitanian.

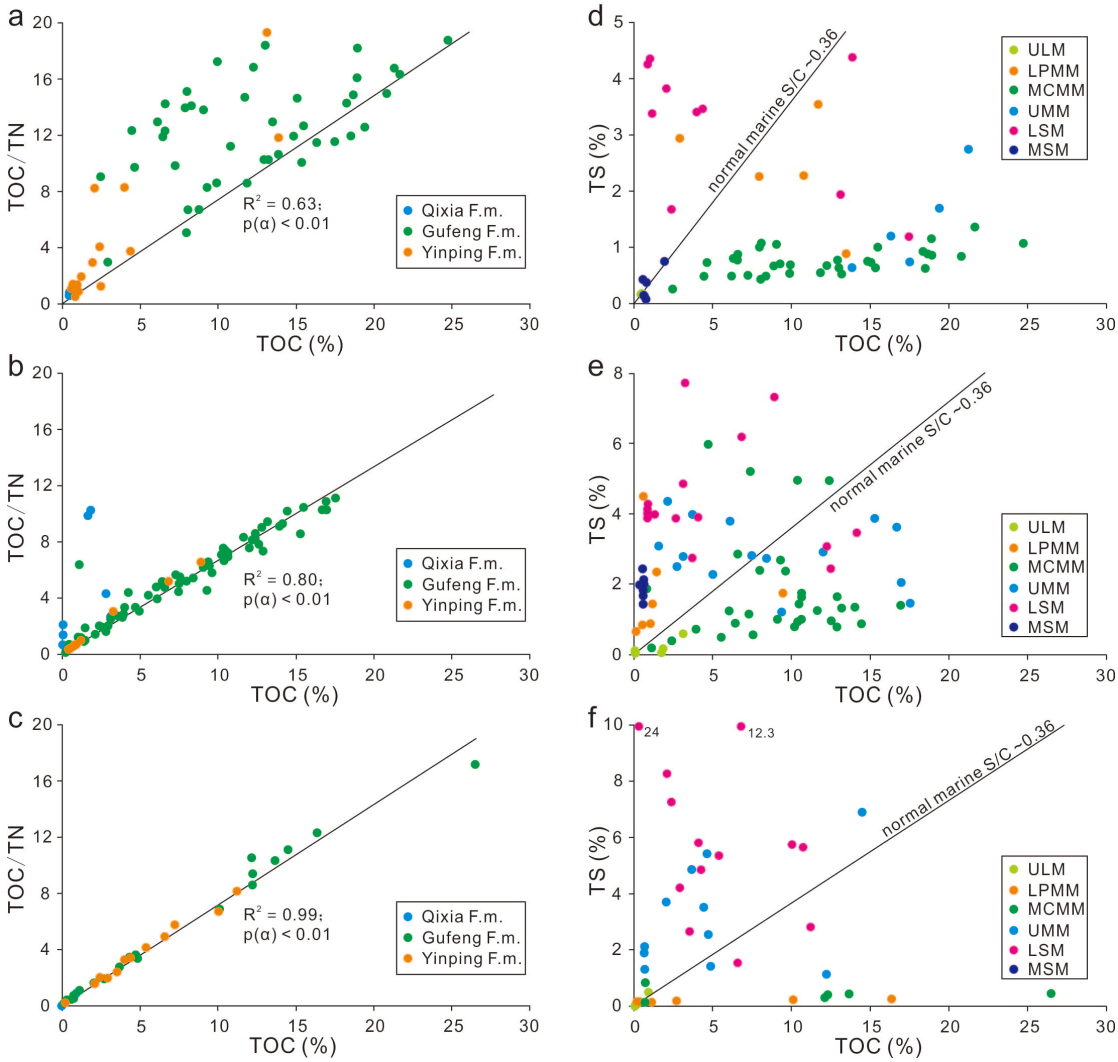

Fig. S2 Crossplots of TOC/TN vs TOC (a, b, c), and TS vs TOC (d, e, f) for the Pingdingshan section, GD core, Qinglongshan section. Abbreviation: F.m.=Formation.

2. Biogeochemical modelling

We modify the model of Shields and Mills (2017) in order to test the potential for the Kamura positive C isotope excursion to be driven by reduced rates of inorganic carbon cycling. Our sole modification to the model is the addition of a strontium cycle, which itself is based on Lenton et al. (2018). Full model equations are reproduced below but the reader is directed to the aforementioned papers for further information.

2.1. Flux calculations

Each flux in the model is defined by a present day rate, *F(0)*, and a set of multipliers that

define dependence of the relative rate on other model variables. This follows the approaches used in the most common biogeochemical box models for Phanerozoic climate. Carbonate and Silicate weathering (F_{wc} and $F_{sil\ weathering}$) are assumed to have a temperature dependence as described in the GEOCARB models (e.g. Berner, 1994; 2006), with the linear functional form for relative river runoff rate approximated with an exponential to avoid nonphysical negative values when temperature is low. Dependence of weathering rates on the relative erosion rate (U) follows Li and Elderfield (2013), with a weaker dependence for silicate weathering, as observed in field studies (Jacobson and Blum, 2003). The dependence of carbonate weathering rate on the crustal carbonate inventory, C, follows the original COPSE model (Bergman et al. 2004). Here T is temperature in Kelvin.

$$F_{wc} = F_{wc}(0) \times U^{0.9} \times \frac{C}{C(0)} \times e^{0.05(T-288)} \quad (1)$$

$$F_{sil\ weathering} = F_{sil\ weathering}(0) \times U^{0.33} \times e^{7537.69\frac{T-288}{288T}} \times (e^{0.03(T-288)})^{0.65} \quad (2)$$

Weathering of organic carbon (F_{wg}) depends on the relative uplift/erosion rate U, and on the relative abundance of organic carbon in the crust (G). Degassing of organic carbon (F_{mg}), and degassing of carbonates (F_{mc}) are assumed to depend on the crustal inventories of these species, and the material subduction rate, termed D. These follow COPSE.

$$F_{wg} = F_{wg}(0) \times U^{0.9} \times \frac{G}{G(0)} \quad (3)$$

$$F_{mg} = F_{mg}(0) \times D \times \frac{G}{G(0)} \quad (4)$$

$$F_{mc} = F_{mc}(0) \times D \times \frac{C}{C(0)} \quad (5)$$

Burial of organic carbon follows the COPSE model, wherein carbon burial scales with bulk sedimentation rate, which has a quadratic dependence on phosphate-limited primary production (Bergman et al. 2004; Vancappellen and Ingall, 1996; Lenton and Watson, 2000).

$$F_{bg} = F_{bg}(0) \times \left(\frac{P}{P(0)}\right)^2 \quad (6)$$

Burial of carbonates (F_{bc}) follows the assumption of long-term alkalinity balance, in which delivery from silicate and carbonate weathering must equal removal via carbonate precipitation:

$$F_{bc} = F_{wc} + F_{sil\ weathering} \quad (7)$$

Following the COPSE model, it is assumed that phosphorus input from weathering is related to the relative rates of silicate, carbonate and organic C weathering.

$$F_{Pinput} = F_{Pinput}(0)\left(\%sil\left(\frac{F_{sil\ weathering}}{F_{sil\ weathering}(0)}\right) + \%carb\left(\frac{F_{wc}}{F_{wc}(0)}\right) + \%org\left(\frac{F_{wg}}{F_{wg}(0)}\right)\right) \quad (8)$$

Here *%sil*, *%carb* and *%org* are the fractions of present day P weathering from each rock type. Following Shields and Mills (2017), we set $\%sil = 0.58, \%carb = 0.21, \%org = 0.21$. Output of P from the surface system via Sedimentary phosphorus burial is modelled with a single term, dependent on organic C burial rate:

$$F_{poutput} = F_{poutput}(0) \times \left(\frac{F_{bg}}{F_{bg}(0)}\right) \quad (9)$$

2.2. Reservoir calculations

Model reservoirs are atmosphere-ocean carbon (A), marine phosphorus (P), crustal carbonate (C) and crustal organic carbon (G). Their sizes are determined by summing their respective sources and sinks:

$$\frac{dA}{dt} = F_{wg} + F_{wc} + F_{mg} + F_{mc} - F_{bg} - F_{bc} \quad (10)$$

$$\frac{dG}{dt} = F_{bg} - F_{wg} - F_{mg} \quad (11)$$

$$\frac{dC}{dt} = F_{bc} - F_{wc} - F_{mc} \quad (12)$$

$$\frac{dP}{dt} = F_{pinput} - F_{poutput} \quad (13)$$

In order to track the isotope composition of each carbon reservoir (δR, its δ^{13}C value), the quantity $R \times \delta R$ is calculated for each reservoir R. δ^{13}C is then calculated by dividing the $R \times \delta R$ value by the size of the reservoir. ΔB represents photosynthetic fractionation and is set at 29‰.

$$\frac{d(A\delta A)}{dt} = F_{wg} \times \delta G + F_{wc} \times \delta C + F_{mg} \times \delta G + F_{mc} \times \delta C$$
$$-F_{bg} \times (\delta A - \Delta B) - F_{bc} \times \delta A \quad (14)$$

$$\frac{d(G \times \delta G)}{dt} = F_{bg} \times (\delta A - \Delta B) - F_{wg} \times \delta G - F_{mg} \times \delta G \quad (15)$$

$$\frac{d(C \times \delta C)}{dt} = F_{bc} \times \delta A - F_{wc} \times \delta C - F_{mc} \times \delta C \quad (16)$$

2.3. Parameter values

Size of reservoirs at present day follows Shileds and Mills (2017). We do not consider 'rapid recycling' of isotope signals in this paper, as the effects are minimal over <10 Myr timescales (Shields and Mills, 2017):

$$A(0) = 3.193 \times 10^{18} \text{ mol} \quad (17)$$

$$G(0) = 1.25 \times 10^{21} \text{ mol} \quad (18)$$

$$C(0) = 5 \times 10^{21} \text{ mol} \quad (19)$$

$$P(0) = 3.1 \times 10^{15} \text{ mol P} \quad (20)$$

$$\delta A(0) = 0 \text{ ‰} \quad (21)$$

$$\delta G(0) = -27 \text{ ‰} \quad (22)$$

$$\delta C(0) = 0 \text{ ‰} \quad (23)$$

The magnitude of present day carbon fluxes is taken from an assessment of the current literature, taking average values (see Shields and Mills, 2017):

$$F_{bg}(0) = 9\times10^{12} \text{ mol yr}^{-1} \quad (24)$$

$$F_{wg}(0) = 7.75\times10^{12} \text{ mol yr}^{-1} \quad (25)$$

$$F_{mg}(0) = 1.25\times10^{12} \text{ mol yr}^{-1} \quad (26)$$

$$F_{wc}(0) = 24\times10^{12} \text{ mol yr}^{-1} \quad (27)$$

$$F_{mc}(0) = 8\times10^{12} \text{ mol yr}^{-1} \quad (28)$$

$$F_{sil\ weathering}(0) = 8\times10^{12} \text{ mol yr}^{-1} \quad (29)$$

P outputs are assumed to equal inputs at the present day (pre-industrial).

$$F_{pinput}(0) = 4.7\times10^{10} \text{ mol yr}^{-1} \quad (30)$$

$$F_{poutput}(0) = 4.7\times10^{10} \text{ mol yr}^{-1} \quad (31)$$

2.4. Temperature approximation

The CO_2 and temperature approximation follows Caldeira and Kasting (1992). This calculation takes into account the solar insolation (fixed here), atmospheric pCO_2, and a dynamic albedo function. A small correction, *tempcorrect*, is made to give T(0) = 288K, as in COPSE, and average surface temperature is calculated from the black body equation, where σ is the Stefan-Boltzmann constant.

$$pCO_2 = \frac{A}{A(0)}\times280\times10^{-6} \quad (32)$$

$$\text{SOLAR} = 1368 \text{ W m}^{-2} \quad (33)$$

$$\text{ALBEDO} = 1.4891 - 0.0065979\times\text{T} + (8.567\times10^{-6})T^2 \quad (34)$$

$$tempcorrect = 0.194 \quad (35)$$

$$\sigma = 5.67\times10^{-8} \text{ W m}^{-2}\text{K}^{-4} \quad (36)$$

$$T_{CO2} = 815.17 + (4.895\times10^{7})T^{-2} - (3.9787\times10^{5})T^{-1} - 6.7084(\log(\text{CO2atm}))^{-2} + 73.221(\log(\text{CO2atm}))^{-1} - 30882T^{-1}(\log(\text{CO2atm}))^{-1} \quad (37)$$

$$T = \left(\frac{SOLAR(1-ALBEDO)}{4\sigma}\right)^{1/4} + T_{CO2} + tempcorrect \quad (38)$$

2.5. Strontium cycle

The strontium fluxes and strontium isotope calculations follow exactly those in Lenton et al. (2018), with the omission of seafloor weathering, which is not included in either the carbon or strontium cycle here. In order to apply the strontium cycle, the model must calculate weathering rates of both basalts and granites. This is achieved for this work by assuming a constant 'basaltic fraction' of silicate weathering, chosen in order to reproduce the baseline $^{87}Sr/^{86}Sr$ ratio at around 270-265 Ma.

$$basfrac = 0.575 \quad (39)$$

$$basw = F_{sil\,weathering} \cdot basfrac \quad (40)$$

$$granw = F_{sil\,weathering}(1 - basfrac) \quad (41)$$

2.5.1. Strontium Fluxes

Mantle Sr Input: $$Sr_{mantle} = k_{Srmantle} \cdot D \quad (42)$$

Basalt Weathering Input: $$Sr_{basw} = k_{Srbasw} \cdot \frac{basw}{basw(0)} \quad (43)$$

Granite Weathering Input: $$Sr_{granw} = k_{Srgranw} \cdot \frac{granw}{granw(0)} \quad (44)$$

Inputs from Carbonate Sediments: $$Sr_{sedw} = k_{Srsedw} \cdot \frac{F_{wc}}{F_{wc}(0)} \cdot \frac{SSr}{SSr_0} \quad (45)$$

Burial in Carbonate Sediments: $Sr_{sedb} = k_{Srsedb} \cdot \frac{F_{bc}}{F_{bc}(0)} \cdot \frac{OSr}{OSr_0}$ (46)

Output from Metamorphism: $Sr_{metam} = k_{Srmetam} \cdot D \cdot \frac{SSr}{SSr_0}$ (47)

2.5.2. Strontium parameters

Mantle Sr Input: $k_{Srmantle} = 7.3\times10^9$ mol yr^{-1} (48)

Total Silicate Weathering Input: $k_{Srsilw} = 13\times10^9$ mol yr^{-1} (49)

Basalt Weathering Input: $k_{Srbasw} = k_{Srsilw} \cdot basfrac$ (50)

Granite Weathering Input: $k_{Srgranw} = k_{Srsilw} \cdot (1 - basfrac)$ (51)

Inputs from Carbonate Sediments: $k_{Srsedw} = 17\times10^9$ mol yr^{-1} (52)

Burial in Carbonate Sediments: $k_{Srsedb} = k_{Srgranw} + k_{Srbasw} + k_{Srmantle} + k_{Srsedw}$ (53)

Output from Metamorphism: $k_{Srmetam} = 13\times10^9$ mol yr^{-1} (54)

2.5.3. Rubidium decay

Decay of ^{87}Rb to ^{87}Sr influences the ^{87}Sr/^{86}Sr ratio over long timescales (and is responsible for the differing ^{87}Sr/^{86}Sr values between different rock types). The decay process is represented explicitly in the model:

$$^{87}Sr/^{86}Sr_{granite} = {}^{87}Sr/^{86}Sr_0 + {}^{87}Rb/^{86}Sr_{granite}\left(1 - e^{-\lambda t}\right) \quad (55)$$

$$^{87}Sr/^{86}Sr_{basalt} = {}^{87}Sr/^{86}Sr_0 + {}^{87}Rb/^{86}Sr_{basalt}\left(1 - e^{-\lambda t}\right) \quad (56)$$

$$^{87}Sr/^{86}Sr_{mantle} = {}^{87}Sr/^{86}Sr_0 + {}^{87}Rb/^{86}Sr_{mantle}\left(1 - e^{-\lambda t}\right) \quad (57)$$

Where time (*t*) is in years from Earth formation (taken to be 4.5 billion years ago). For each rock type, the rubidium-strontium ratio is then calculated such that the observed present day ^{87}Sr/^{86}Sr ratio is achieved for each rock type after 4.5 billion years:

$$^{87}Rb/^{86}Sr = \frac{\left({}^{87}Sr/^{86}Sr_{present} - {}^{87}Sr/^{86}Sr_0\right)}{\left(1 - e^{-\lambda \cdot 4.5\times10^9}\right)} \quad (58)$$

2.5.4. Reservoir calculations

Strontium reservoir calculations follow Lenton et al. (2018), where *OSr* is ocean strontium and *SSr*

is sediment strontium abundance in moles:

$$\frac{dOSr}{dt} = Sr_{granw} + Sr_{basw} + Sr_{sedw} + Sr_{mantle} - Sr_{sedb} \qquad (59)$$

$$\frac{dSSr}{dt} = Sr_{sedb} - Sr_{sedw} - Sr_{metam} \qquad (60)$$

2.5.5. $^{87}Sr/^{86}Sr$ calculations

The isotopic composition of the ocean and the sediments are calculated by first creating reservoirs consisting of Sr concentrations multiplied by their isotopic ratios, where δSr_X denotes the $^{87}Sr/^{86}Sr$ ratio of reservoir *X*:

$$\frac{d(OSr \cdot \delta Sr_{ocean})}{dt} = Sr_{granw} \cdot \delta Sr_{granite} + Sr_{basw} \cdot \delta Sr_{basalt} + Sr_{sedw} \cdot \delta Sr_{sediment} + Sr_{mantle} \cdot \delta Sr_{mantle} - Sr_{sedb} \cdot \delta Sr_{ocean} \qquad (61)$$

$$\frac{d(SSr \cdot \delta Sr_{sediment})}{dt} = Sr_{sedb} \cdot \delta Sr_{ocean} - Sr_{sedw} \cdot \delta Sr_{sediment} - Sr_{metam} \cdot \delta Sr_{sediment} \qquad (61)$$

The ocean $^{87}Sr/^{86}Sr$ ratio is calculated by dividing the new reservoir by the known concentration:

$$\delta Sr_{ocean} = \frac{OSr \cdot \delta Sr_{ocean}}{OSr} \qquad (63)$$

The carbonate sediment $^{87}Sr/^{86}Sr$ ratio includes an additional term to account for rubidium decay within the sedimentary reservoir:

$$\delta Sr_{sediment} = \frac{SSr \cdot \delta Sr_{sediment}}{SSr} + {}^{87}Rb/{}^{86}Sr_{carbonate}\left(1 - e^{-\lambda \Delta t}\right) \qquad (64)$$

References

Bergman, N. M., Lenton, T. M. & Watson, A. J. {COPSE}: A new model of biogeochemical cycling over Phanerozoic time. *American Journal of Science* **304**, 397-437 (2004).

Berner, R. A. Geocarb II: A revised model of atmospheric CO_2 over Phanerozoic time. *American Journal of Science* **294**, 56-91 (1994).

Berner, R. A. GEOCARBSULF: A combined model for Phanerozoic atmospheric O_2 and CO_2 *Geochimica et Cosmochimica Acta* **70**, 5653-5664 (2006).

Caldeira, K. & Kasting, J. F. The life span of the biosphere revisited. *Nature* **360**, 721-723 (1992).

Jacobson AD, Blum JD (2003) Relationship between mechanical erosion and atmospheric CO_2 consumption in the New Zealand Southern Alps. *Geology* 31: 865-868.

Lenton, T. M., Daines, S. J. & Mills, B. J. W. COPSE reloaded: An improved model of biogeochemical cycling over Phanerozoic time. *Earth-Sci. Rev.* **178**, 1-28, doi:10.1016/j.earscirev.2017.12.004 (2018).

Lenton, T. M. & Watson, A. J. Redfield revisited: I. Regulation of nitrate, phosphate and oxygen in the ocean. *Global Biogeochemical Cycles.* **14**, 225-248 (2000).

Li, G. & Elderfield, H. Evolution of carbon cycle over the past 100 million years. *Geochimica et Cosmochimica Acta* **103**, 11-25, doi:10.1016/j.gca.2012.10.014 (2013)

Shields, G. A. & Mills, B. J. W. Tectonic controls on the long-term carbon isotope mass balance. *Proceedings of the National Academy of Sciences of the United States of America* **114**, 4318-4323, doi:10.1073/pnas.1614506114 (2017).

VanCappellen, P. & Ingall, E. D. Redox stabilization of the atmosphere and oceans by phosphorus-limited marine productivity. *Science* **271**, 493-496 (1996).

3. Table

Table S1 Geochemistry data of the GD core, Qinglongshan section and Pingdingshan section

Sample	Section/core	Formation	Member	Lithology	Biozone	Depth (m)	Al (%)	TOC (%)	TN (%)	TS (%)	TS/TOC	TOC/TN	$\delta^{13}C_{org}$(‰)
CSC-P1q-7	Pingdingshan	Qixia	ULM	Limestone	*Parafusulina multiseptata*	-3.00	0.24	0.56	0.75	0.18	0.32	0.75	-27.73
CSC-P1q-5	Pingdingshan	Qixia	ULM	Limestone	*Parafusulina multiseptata*	-2.00	0.23	0.63	0.62	0.13	0.21	1.02	-27.74
CSC-P1q-3	Pingdingshan	Qixia	ULM	Limestone	*Parafusulina multiseptata*	-1.00	0.27	0.49	0.58	0.16	0.33	0.85	-27.62
CSC-P1q-2	Pingdingshan	Qixia	ULM	Limestone	*Parafusulina multiseptata*	-0.50	0.25	0.44	0.69	0.17	0.38	0.64	-27.92
CSC-P2g-1	Pingdingshan	Gufeng	LPMM	Mudstone	*Jinogondolella nankingensis*	0.05	8.59	2.91	0.97	2.94	1.01	3.00	-25.47
CSC-P2g-5	Pingdingshan	Gufeng	LPMM	Mudstone	*Jinogondolella nankingensis*	0.40	6.66	7.96	1.56	2.26	0.28	5.09	-26.38
CSC-P2g-9	Pingdingshan	Gufeng	LPMM	Mudstone	*Jinogondolella nankingensis*	0.90	4.30	13.49	1.04	0.89	0.07	12.97	-26.04
CSC-P2g-13	Pingdingshan	Gufeng	LPMM	Mudstone	*Jinogondolella nankingensis*	1.50	3.52	11.70	0.80	3.54	0.30	14.69	-26.23
CSC-P2g-17	Pingdingshan	Gufeng	LPMM	Mudstone	*Jinogondolella nankingensis*	2.30	3.23	10.79	0.96	2.28	0.21	11.21	-27.11
CSC-P2g-21	Pingdingshan	Gufeng	MCMM	Mudstone	*Pseudoalbaillella longtanensis*–*Pseudoalbaillella fusiformis*	3.20	5.05	9.29	1.12	0.78	0.08	8.31	-26.71
CSC-P2g-24	Pingdingshan	Gufeng	MCMM	Siliceous mudstone	*Pseudoalbaillella longtanensis*–*Pseudoalbaillella fusiformis*	4.20	0.72	2.46	0.27	0.26	0.11	9.07	-27.24
CSC-P2g-27	Pingdingshan	Gufeng	MCMM	Chert	*Pseudoalbaillella longtanensis*–*Pseudoalbaillella fusiformis*	5.10	0.86	6.10	0.47	0.48	0.08	12.97	-26.84
CSC-P2g-30	Pingdingshan	Gufeng	MCMM	Chert	*Pseudoalbaillella longtanensis*–*Pseudoalbaillella fusiformis*	6.00	0.90	4.46	0.36	0.49	0.11	12.35	-27.28
CSC-P2g-33	Pingdingshan	Gufeng	MCMM	Siliceous	*Pseudoalbaillella*	7.00	1.67	12.25	0.73	0.68	0.06	16.82	-27.29

				mudstone	*longtanensis*– *Pseudoalbaillella fusiformis*								
CSC-P2g-35	Pingdingshan	Gufeng	MCMM	Siliceous mudstone	*Follicucullus monacanthus*	8.00	1.67	13.02	0.71	0.64	0.05	18.39	-26.42
CSC-P2g-37	Pingdingshan	Gufeng	MCMM	Chert	*Follicucullus monacanthus*	9.00	1.21	9.94	0.58	0.69	0.07	17.25	-27.29
CSC-P2g-40	Pingdingshan	Gufeng	MCMM	Chert	*Follicucullus monacanthus*	10.00	0.96	6.32	0.53	0.81	0.13	12.03	-27.67
CSC-P2g-43	Pingdingshan	Gufeng	MCMM	Chert	*Follicucullus monacanthus*	10.90	1.17	4.63	0.48	0.73	0.16	9.74	-27.48
CSC-P2g-46	Pingdingshan	Gufeng	MCMM	Chert	*Follicucullus monacanthus*	11.70	1.47	9.06	0.66	1.06	0.12	13.79	-27.70
CSC-P2g-49	Pingdingshan	Gufeng	MCMM	Chert	*Follicucullus monacanthus*	12.70	0.85	7.99	0.53	1.06	0.13	15.13	-28.02
CSC-P2g-52	Pingdingshan	Gufeng	MCMM	Chert	*Follicucullus monacanthus*	13.80	0.87	7.97	0.56	1.04	0.13	14.12	-28.01
CSC-P2g-54	Pingdingshan	Gufeng	MCMM	Chert	*Follicucullus monacanthus*	14.60	0.77	6.60	0.46	0.88	0.13	14.24	-27.60
CSC-P2g-56	Pingdingshan	Gufeng	MCMM	Chert	*Follicucullus monacanthus*	15.50	0.80	6.58	0.53	0.80	0.12	12.33	-27.81
CSC-P2g-58	Pingdingshan	Gufeng	MCMM	Chert	*Follicucullus monacanthus*	16.40	1.44	8.40	0.60	0.51	0.06	14.12	-26.44
CSC-P2g-60	Pingdingshan	Gufeng	MCMM	Siliceous mudstone	*Follicucullus monacanthus*	17.30	2.83	18.90	1.17	1.16	0.06	16.10	-26.09
CSC-P2g-62	Pingdingshan	Gufeng	MCMM	Chert	*Follicucullus monacanthus*	18.00	1.37	7.24	0.73	0.53	0.07	9.86	-26.86
CSC-P2g-65	Pingdingshan	Gufeng	MCMM	Siliceous mudstone	*Follicucullus monacanthus*	18.80	2.48	15.06	1.03	0.74	0.05	14.65	-26.18
CSC-P2g-67	Pingdingshan	Gufeng	MCMM	Siliceous mudstone	*Follicucullus monacanthus*	19.60	2.03	18.93	1.04	0.86	0.05	18.19	-26.49
CSC-P2g-68	Pingdingshan	Gufeng	MCMM	Siliceous mudstone	*Follicucullus monacanthus*	20.00	3.02	24.73	1.32	1.07	0.04	18.77	-26.05
CH-1	Pingdingshan	Gufeng	MCMM	Siliceous mudstone	*Follicucullus monacanthus*	21.20	1.40	14.84	1.24	0.75	0.05	11.96	-26.00
CH-3	Pingdingshan	Gufeng	MCMM	Chert	*Follicucullus monacanthus*	21.60	0.66	12.93	1.26	0.77	0.06	10.29	-26.50
CH-7	Pingdingshan	Gufeng	MCMM	Chert	*Follicucullus scholasticus*–	22.40	1.73	11.85	1.38	0.55	0.05	8.62	-27.50

CH-9	Pingdingshan	Gufeng	MCMM	Siliceous mudstone	*Ruzhencevispongus uralicus* *Follicucullus scholasticus*– *Ruzhencevispongus uralicus*	22.85	2.71	9.90	1.15	0.54	0.05	8.63	-25.90
CH-10	Pingdingshan	Gufeng	MCMM	Siliceous mudstone	*Follicucullus scholasticus*– *Ruzhencevispongus uralicus*	23.00	2.35	18.37	1.28	0.93	0.05	14.31	-26.20
CH-14	Pingdingshan	Gufeng	MCMM	Siliceous mudstone	*Follicucullus scholasticus*– *Ruzhencevispongus uralicus*	23.20	4.75	15.47	1.22	1.02	0.07	12.69	-26.60
CH-17	Pingdingshan	Gufeng	MCMM	Chert	*Follicucullus scholasticus*– *Ruzhencevispongus uralicus*	23.70	1.26	8.76	1.30	0.67	0.08	6.73	-26.80
CH-19	Pingdingshan	Gufeng	MCMM	Siliceous mudstone	*Follicucullus scholasticus*– *Ruzhencevispongus uralicus*	24.30	2.48	21.65	1.32	1.36	0.06	16.35	-26.70
CH-21	Pingdingshan	Gufeng	MCMM	Siliceous mudstone	*Follicucullus scholasticus*– *Ruzhencevispongus uralicus*	24.70	2.48	18.66	1.23	0.89	0.05	15.14	-26.90
CH-23	Pingdingshan	Gufeng	MCMM	Siliceous mudstone	*Follicucullus scholasticus*– *Ruzhencevispongus uralicus*	25.05	2.19	20.80	1.39	0.84	0.04	14.96	-25.32
CH-27	Pingdingshan	Gufeng	MCMM	Siliceous mudstone	*Follicucullus scholasticus*– *Ruzhencevispongus uralicus*	25.45	2.71	15.35	1.52	0.64	0.04	10.08	-25.55
CH-32	Pingdingshan	Gufeng	MCMM	Chert	*Follicucullus scholasticus*– *Ruzhencevispongus uralicus*	26.00	2.67	8.05	1.20	0.44	0.05	6.70	-26.24
CH-38	Pingdingshan	Gufeng	MCMM	Siliceous mudstone	*Follicucullus scholasticus*– *Ruzhencevispongus uralicus*	26.60	3.77	18.50	1.55	0.63	0.03	11.97	-25.61
CH-41	Pingdingshan	Gufeng	MCMM	Chert	*Follicucullus scholasticus*– *Ruzhencevispongus uralicus*	27.10	2.09	13.20	1.28	0.53	0.04	10.34	-25.69
CH-46	Pingdingshan	Gufeng	UMM	Mudstone		28.00	2.57	19.40	1.54	1.70	0.09	12.56	-25.67
CH-50	Pingdingshan	Gufeng	UMM	Mudstone		28.75	2.33	16.32	1.42	1.21	0.07	11.47	-25.88
CH-54	Pingdingshan	Gufeng	UMM	Mudstone		29.45	3.01	17.46	1.51	0.73	0.04	11.57	-25.77

CH-57	Pingdingshan	Gufeng	UMM	Mudstone	30.00	8.27	13.86	1.30	0.64	0.05	10.66	-26.04
CH-60	Pingdingshan	Gufeng	UMM	Mudstone	30.80	4.58	21.24	1.27	2.74	0.13	16.73	-25.85
GS-1	Pingdingshan	Yinping	LSM	Shale	31.00	6.94	17.47	0.83	1.19	0.07	21.04	-25.97
CH-63	Pingdingshan	Yinping	LSM	Shale	31.30	5.65	13.87	1.17	4.38	0.32	11.82	-25.92
GS-3	Pingdingshan	Yinping	LSM	Shale	31.40	6.33	2.07	0.25	3.82	1.85	8.23	-26.11
CH-67	Pingdingshan	Yinping	LSM	Shale	31.80	6.49	4.37	1.17	3.46	0.79	3.75	-25.48
GS-5	Pingdingshan	Yinping	LSM	Shale	31.85	8.17	13.13	0.68	1.94	0.15	19.29	-25.27
GS-7	Pingdingshan	Yinping	LSM	Shale	32.10	10.61	3.98	0.48	3.41	0.85	8.29	-24.51
CH-71	Pingdingshan	Yinping	LSM	Shale	32.50	11.58	0.88	1.20	4.25	4.85	0.73	-24.77
CH-74	Pingdingshan	Yinping	LSM	Shale	33.20	11.44	1.03	1.10	4.35	4.24	0.94	-24.68
GS-11	Pingdingshan	Yinping	LSM	Shale	33.40	12.69	2.39	0.59	1.68	0.70	4.09	-24.39
GS-13	Pingdingshan	Yinping	LSM	Shale	33.80	13.22	1.16	0.57	3.38	2.91	2.03	-24.91
GS-15	Pingdingshan	Yinping	MSM	Shale	34.40	13.44	0.67	0.58	0.13	0.20	1.16	-23.91
GS-18	Pingdingshan	Yinping	MSM	Shale	35.30	13.55	0.73	0.55	0.11	0.15	1.33	-23.34
GS-21	Pingdingshan	Yinping	MSM	Shale	36.10	13.36	1.94	0.65	0.75	0.39	2.97	-23.63
GS-25	Pingdingshan	Yinping	MSM	Shale	37.50	14.07	0.58	0.62	0.43	0.74	0.93	-23.48
GS-28	Pingdingshan	Yinping	MSM	Shale	38.50	13.18	0.80	0.59	0.38	0.47	1.36	-23.36
GD1-P2g-1	GD	Qixia	ULM	Limestone	1244.19	0.12	0.08	0.06	0.04	0.53	1.41	-28.53
GD1-P2g-2	GD	Qixia	ULM	Nodular Chert	1243.00	0.53	3.13	1.16	0.59	0.19	2.71	-25.78
GD1-P2g-3	GD	Qixia	ULM	Limestone	1241.80	0.13	1.67	0.17	0.01	0.01	9.86	-26.67
GD1-P2g-4	GD	Qixia	ULM	Limestone	1238.78	0.11	0.06	0.09	0.01	0.15	0.67	-28.46
GD1-P2g-5	GD	Qixia	ULM	Limestone	1237.51	0.58	1.86	0.18	0.18	0.10	10.28	-26.92
GD1-P2g-7	GD	Qixia	ULM	Limestone	1234.90	0.14	0.09	0.04	0.06	0.72	2.13	-27.93
GD1-P2g-8	GD	Gufeng	LPMM	Mudstone	1234.40	3.52	0.54	0.70	0.85	1.58	0.76	-25.84

GD1-P2g-10	GD	Gufeng	LPMM	Mudstone	1232.90	5.24	1.05	0.84	0.89	0.85	1.25	-25.90
GD1-P2g-12	GD	Gufeng	LPMM	Mudstone	1231.20	4.06	0.14	0.57	0.66	4.78	0.25	-25.72
GD1-P2g-14	GD	Gufeng	LPMM	Mudstone	1230.10	5.64	1.18	0.94	1.45	1.23	1.26	-26.48
GD1-P2g-16	GD	Gufeng	LPMM	Mudstone	1228.30	7.10	0.59	1.19	4.50	7.57	0.50	-24.60
GD1-P2g-18	GD	Gufeng	LPMM	Mudstone	1226.87	2.49	9.47	1.43	1.75	0.18	6.60	-25.39
GD1-P2g-20	GD	Gufeng	LPMM	Mudstone	1225.40	4.18	1.44	0.72	2.35	1.64	1.99	-25.76
GD1-P2g-21	GD	Gufeng	MCMM	Chert	1225.00	0.68	3.95	1.34	0.73	0.18	2.96	-26.45
GD1-P2g-22	GD	Gufeng	MCMM	Chert	1224.60	0.80	7.31	1.29	1.16	0.16	5.68	-26.19
GD1-P2g-23	GD	Gufeng	MCMM	Chert	1224.00	3.37	8.00	1.53	2.40	0.30	5.23	-25.75
GD1-P2g-24	GD	Gufeng	MCMM	Chert	1223.60	0.79	5.55	1.31	0.50	0.09	4.22	-25.61
GD1-P2g-25	GD	Gufeng	MCMM	Chert	1222.80	0.60	2.40	1.14	0.40	0.17	2.11	-26.22
GD1-P2g-26	GD	Gufeng	MCMM	Limestone	1222.10	0.41	1.12	0.18	0.20	0.18	6.40	-26.75
GD1-P2g-27	GD	Gufeng	MCMM	mudstone	1221.40	13.18	0.83	2.14	1.90	2.29	0.39	-24.76
GD1-P2g-28	GD	Gufeng	MCMM	Siliceous mudstone	1220.80	2.87	10.57	1.53	1.79	0.17	6.93	-26.14
GD1-P2g-29	GD	Gufeng	MCMM	Siliceous mudstone	1220.20	2.23	10.65	1.49	1.05	0.10	7.13	-27.33
GD1-P2g-30	GD	Gufeng	MCMM	Siliceous mudstone	1219.60	2.05	9.09	1.45	1.04	0.11	6.26	-26.49
GD1-P2g-31	GD	Gufeng	MCMM	Chert	1218.80	0.87	7.57	1.37	0.57	0.08	5.53	-27.31
GD1-P2g-32	GD	Gufeng	MCMM	Chert	1218.30	1.09	10.20	1.41	0.80	0.08	7.23	-26.77
GD1-P2g-33	GD	Gufeng	MCMM	Chert	1217.20	1.56	6.05	1.26	1.25	0.21	4.82	-26.89
GD1-P2g-34	GD	Gufeng	MCMM	Chert	1216.70	1.79	6.44	1.24	0.90	0.14	5.20	-26.46
GD1-P2g-35	GD	Gufeng	MCMM	Siliceous mudstone	1216.10	6.18	12.91	1.75	1.65	0.13	7.36	-27.00
GD1-P2g-36	GD	Gufeng	MCMM	Siliceous	1215.26	3.28	10.66	1.53	1.64	0.15	6.97	-26.61

				mudstone								
GD1-P2g-37	GD	Gufeng	MCMM	Siliceous mudstone	1214.56	1.55	13.20	1.40	1.33	0.10	9.46	-27.44
GD1-P2g-38	GD	Gufeng	MCMM	Mudstone	1214.10	7.50	4.72	1.40	5.98	1.27	3.37	-26.65
GD1-P2g-39	GD	Gufeng	MCMM	Mudstone	1213.56	6.10	9.63	1.65	2.38	0.25	5.83	-26.65
GD1-P2g-40	GD	Gufeng	MCMM	Mudstone	1213.10	10.63	9.31	2.04	2.69	0.29	4.57	-27.54
GD1-P2g-41	GD	Gufeng	MCMM	Mudstone	1212.30	4.91	7.52	1.49	5.21	0.69	5.06	-25.88
GD1-P2g-42	GD	Gufeng	MCMM	Mudstone	1211.60	4.60	10.39	1.55	4.96	0.48	6.70	-25.70
GD1-P2g-43	GD	Gufeng	MCMM	Siliceous mudstone	1210.80	3.79	12.41	1.42	4.95	0.40	8.74	-26.42
GD1-P2g-44	GD	Gufeng	MCMM	Siliceous mudstone	1210.00	3.90	6.60	1.37	2.86	0.43	4.83	-26.16
GD1-P2g-45	GD	Gufeng	MCMM	Siliceous mudstone	1209.30	2.93	11.65	1.40	1.26	0.11	8.34	-26.73
GD1-P2g-46	GD	Gufeng	MCMM	Siliceous mudstone	1208.60	2.38	12.41	1.49	0.97	0.08	8.31	-26.72
GD1-P2g-47	GD	Gufeng	MCMM	Chert	1208.10	2.19	10.36	1.37	0.97	0.09	7.55	-25.82
GD1-P2g-48	GD	Gufeng	MCMM	Siliceous mudstone	1207.50	3.88	14.04	1.51	1.35	0.10	9.30	-25.95
GD1-P2g-49	GD	Gufeng	MCMM	Siliceous mudstone	1206.70	2.98	10.49	1.42	1.44	0.14	7.39	-25.47
GD1-P2g-50	GD	Gufeng	MCMM	Siliceous mudstone	1206.00	2.42	14.46	1.42	0.88	0.06	10.21	-25.32
GD1-P2g-51	GD	Gufeng	MCMM	Siliceous mudstone	1205.80	2.80	12.89	1.40	0.79	0.06	9.23	-26.19
GD1-P2g-52	GD	Gufeng	MCMM	Siliceous	1205.60	3.36	16.95	1.56	1.41	0.08	10.88	-25.42

				mudstone								
GD1-P2g-53	GD	Gufeng	UMM	Mudstone	1205.00	8.33	7.48	1.67	2.82	0.38	4.48	-25.25
GD1-P2g-54	GD	Gufeng	UMM	Mudstone	1204.30	4.20	16.70	1.63	3.63	0.22	10.27	-25.70
GD1-P2g-55	GD	Gufeng	UMM	Mudstone	1203.50	5.38	9.39	1.49	1.22	0.13	6.30	-25.75
GD1-P2g-56	GD	Gufeng	UMM	Mudstone	1202.90	7.39	6.11	1.54	3.79	0.62	3.97	-25.87
GD1-P2g-57	GD	Gufeng	UMM	Mudstone	1202.30	7.48	3.12	1.46	2.79	0.89	2.13	-24.80
GD1-P2g-58	GD	Gufeng	UMM	Mudstone	1201.90	8.35	5.01	1.58	2.28	0.46	3.16	-25.91
GD1-P2g-59	GD	Gufeng	UMM	Mudstone	1201.50	9.57	1.48	1.48	2.36	1.60	1.00	-24.91
GD1-P2g-60	GD	Gufeng	UMM	Mudstone	1200.90	9.59	3.77	1.47	3.97	1.05	2.57	-24.65
GD1-P2g-61	GD	Gufeng	UMM	Mudstone	1200.25	6.80	16.98	1.66	2.06	0.12	10.22	-25.82
GD1-P2g-62	GD	Gufeng	UMM	Mudstone	1199.90	9.80	2.15	1.48	4.36	2.03	1.45	-25.08
GD1-P2g-63	GD	Gufeng	UMM	Mudstone	1199.40	7.11	8.43	1.54	2.74	0.32	5.46	-25.53
GD1-P2g-64	GD	Gufeng	UMM	Mudstone	1199.10	5.14	17.56	1.55	1.47	0.08	11.36	-25.56
GD1-P2g-65	GD	Gufeng	UMM	Mudstone	1198.60	6.84	12.02	1.58	2.92	0.24	7.60	-27.24
GD1-P2g-66	GD	Gufeng	UMM	Mudstone	1197.90	6.90	15.30	1.79	3.88	0.25	8.57	-25.40
GD1-P2g-67	GD	Gufeng	UMM	Mudstone	1197.20	9.04	2.73	1.55	2.51	0.92	1.76	-25.00
GD1-P2g-68	GD	Gufeng	UMM	Mudstone	1196.30	10.29	1.57	1.54	3.09	1.97	1.02	-25.60
GD1-P2g-69	GD	Gufeng	UMM	Mudstone	1195.40	9.25	2.57	1.33	3.92	1.52	1.93	-23.90
GD1-P2g-70	GD	Gufeng	UMM	Mudstone	1194.50	8.74	3.13	1.24	4.86	1.55	2.52	-24.30
GD1-P2g-71	GD	Gufeng	UMM	Mudstone	1193.60	8.79	3.71	1.30	2.75	0.74	2.85	-24.10
GD1-P2g-72	GD	Gufeng	UMM	Mudstone	1192.90	8.55	4.07	1.23	3.91	0.96	3.32	-24.70
GD1-P2g-73	GD	Gufeng	UMM	Mudstone	1192.70	9.57	14.16	1.51	3.47	0.24	9.35	-25.20
GD1-P2g-74	GD	Gufeng	UMM	Mudstone	1192.30	10.76	12.51	1.57	2.45	0.20	7.96	-25.60
GD1-P2g-75	GD	Gufeng	UMM	Mudstone	1191.90	9.88	12.26	1.52	3.08	0.25	8.09	-25.40
GD1-P2g-76	GD	Yinping	LSM	Shale	1191.50	7.44	3.30	1.08	7.74	2.35	3.05	-25.50
GD1-P2g-77	GD	Yinping	LSM	Shale	1191.20	9.40	8.92	1.36	7.32	0.82	6.56	-25.10

GD1-P2g-78	GD	Yinping	LSM	Shale		1190.40	9.97	6.85	1.31	6.19	0.90	5.21	-24.80
GD1-P3l-79	GD	Yinping	LSM	Shale		1189.60	12.39	0.91	1.28	4.29	4.69	0.71	-25.20
GD1-P3l-80	GD	Yinping	LSM	Shale		1189.10	12.49	0.82	1.25	3.99	4.86	0.66	-25.50
GD1-P3l-81	GD	Yinping	LSM	Shale		1188.40	11.08	1.24	1.26	3.95	3.18	0.99	-25.60
GD1-P3l-82	GD	Yinping	LSM	Shale		1187.60	12.62	0.77	1.28	3.94	5.08	0.60	-25.40
GD1-P3l-83	GD	Yinping	LSM	Shale		1187.00	12.83	0.89	1.31	4.20	4.70	0.68	-25.70
GD1-P3l-84	GD	Yinping	MSM	Shale		1184.70	12.75	0.59	1.24	1.44	2.46	0.47	-23.70
GD1-P3l-85	GD	Yinping	MSM	Shale		1183.50	12.49	0.58	1.19	1.68	2.88	0.49	-23.90
GD1-P3l-86	GD	Yinping	MSM	Shale		1182.50	11.72	0.59	1.19	1.83	3.11	0.50	-24.21
GD1-P3l-87	GD	Yinping	MSM	Shale		1181.50	12.05	0.55	1.24	2.44	4.46	0.44	-25.34
GD1-P3l-88	GD	Yinping	MSM	Shale		1180.50	10.51	0.42	1.17	1.95	4.64	0.36	-24.23
GD1-P3l-89	GD	Yinping	MSM	Shale		1179.50	12.67	0.58	1.30	2.12	3.66	0.45	-24.21
GD1-P3l-90	GD	Yinping	MSM	Shale		1178.50	12.20	0.62	1.20	2.02	3.26	0.52	-24.43
QLS-2	Qinglongshan	Qixia	ULM	Limestone	*Parafusulina multiseptata*	-9.90	0.14	0.04	1.01	0.01	0.30	0.04	-26.59
QLS-5	Qinglongshan	Qixia	ULM	Limestone	*Parafusulina multiseptata*	-4.24	0.12	0.07	0.96	0.03	0.39	0.08	-27.73
QLS-7	Qinglongshan	Qixia	ULM	Limestone	*Parafusulina multiseptata*	-1.42	0.14	0.05	1.04	0.05	1.01	0.05	-27.35
QLS-9	Qinglongshan	Qixia	ULM	Limestone	*Parafusulina multiseptata*	0.00	0.75	0.05	1.13	0.03	0.57	0.05	-27.99
QLS-10	Qinglongshan	Gufeng	LPMM	Mudstone	*Jinogondolella nankingensis*	0.20	3.49	0.17	1.24	0.16	0.92	0.14	-25.79
QLS-12	Qinglongshan	Gufeng	LPMM	Mudstone	*Jinogondolella nankingensis*	1.16	9.61	2.69	1.40	0.18	0.07	1.92	-25.41
QLS-14	Qinglongshan	Gufeng	LPMM	Chert	*Jinogondolella nankingensis*	2.64	0.20	0.35	0.97	0.16	0.46	0.36	-26.61
QLS-15	Qinglongshan	Gufeng	LPMM	Mudstone	*Jinogondolella nankingensis*	3.47	4.21	16.37	1.33	0.25	0.02	12.33	-26.17
QLS-16	Qinglongshan	Gufeng	LPMM	Mudstone	*Jinogondolella nankingensis*	4.13	5.25	10.11	1.47	0.23	0.02	6.88	-25.75
QLS-17	Qinglongshan	Gufeng	LPMM	Chert	*Jinogondolella nankingensis*	4.62	0.59	1.11	1.01	0.14	0.13	1.10	-24.59
QLS-19	Qinglongshan	Gufeng	MCMM	Chert	*Pseudoalbaillella longtanensis*–	5.29	0.68	0.68	1.01	0.12	0.18	0.67	-26.13

QLS-20	Qinglongshan	Gufeng	MCMM	Chert	*Pseudoalbaillella fusiformis* *Pseudoalbaillella longtanensis*– *Pseudoalbaillella fusiformis*	5.78	0.59	0.69	0.98	0.13	0.19	0.70	-25.74
QLS-21	Qinglongshan	Gufeng	MCMM	Siliceous mudstone	*Follicucullus monacanthus*	6.88	2.59	13.66	1.32	0.43	0.03	10.36	-28.31
QLS-22	Qinglongshan	Gufeng	MCMM	Siliceous mudstone	*Follicucullus monacanthus*	8.18	2.69	12.23	1.30	0.36	0.03	9.39	-26.67
QLS-23	Qinglongshan	Gufeng	MCMM	Siliceous mudstone	*Follicucullus monacanthus*	9.00	1.64	12.12	1.16	0.30	0.02	10.47	-25.67
QLS-24	Qinglongshan	Gufeng	MCMM	Siliceous mudstone	*Follicucullus scholasticus*– *Ruzhencevispongus uralicus*	10.09	3.97	26.51	1.54	0.45	0.02	17.19	-27.42
QLS-25	Qinglongshan	Gufeng	MCMM	Siliceous mudstone	*Follicucullus scholasticus*– *Ruzhencevispongus uralicus*	10.94	12.59	0.74	1.41	0.85	1.15	0.52	-24.40
QLS-26	Qinglongshan	Gufeng	UMM	Mudstone		12.11	12.59	0.64	1.34	1.89	2.97	0.47	-23.55
QLS-27	Qinglongshan	Gufeng	UMM	Mudstone		12.89	9.53	14.49	1.30	6.88	0.47	11.12	-25.47
QLS-29	Qinglongshan	Gufeng	UMM	Mudstone		15.23	9.95	0.66	1.32	2.11	3.21	0.50	-24.44
QLS-31	Qinglongshan	Gufeng	UMM	Mudstone		16.94	14.78	4.85	1.45	1.42	0.29	3.35	-25.00
QLS-33	Qinglongshan	Gufeng	UMM	Mudstone		18.94	10.78	4.63	1.35	5.41	1.17	3.43	-24.45
QLS-35	Qinglongshan	Gufeng	UMM	Mudstone		21.54	11.96	2.04	1.26	3.69	1.81	1.62	-24.19
QLS-37	Qinglongshan	Gufeng	UMM	Mudstone		23.39	8.20	12.21	1.42	1.16	0.10	8.61	-26.67
QLS-39	Qinglongshan	Gufeng	UMM	Mudstone		25.62	12.44	0.68	1.36	1.30	1.93	0.50	-25.20
QLS-40	Qinglongshan	Gufeng	UMM	Mudstone		27.10	13.81	4.42	1.26	3.51	0.79	3.51	-24.27
QLS-41	Qinglongshan	Gufeng	UMM	Mudstone		28.22	14.04	3.66	1.28	4.85	1.33	2.85	-25.05
QLS-43	Qinglongshan	Gufeng	UMM	Mudstone		29.76	13.59	4.71	1.29	2.54	0.54	3.65	-26.96
QLS-45	Qinglongshan	Yinping	LSM	Calcareous		31.48	4.52	7.23	1.25	12.31	1.70	5.79	-25.14

				shale								
QLS-46	Qinglongshan	Yinping	LSM	Calcareous shale	32.34	1.93	0.18	1.20	24.00	132.07	0.15	-25.46
QLS-47	Qinglongshan	Yinping	LSM	Shale	32.43	12.17	2.37	1.14	7.25	3.06	2.08	-25.11
QLS-48	Qinglongshan	Yinping	LSM	Shale	33.21	13.31	4.25	1.26	4.84	1.14	3.37	-25.87
QLS-49	Qinglongshan	Yinping	LSM	Calcareous shale	34.15	4.66	10.04	1.50	5.73	0.57	6.71	-26.50
QLS-50	Qinglongshan	Yinping	LSM	Calcareous shale	34.50	0.61	2.09	1.46	8.25	3.95	1.44	-26.99
QLS-51	Qinglongshan	Yinping	LSM	Shale	35.79	12.82	3.52	1.46	2.65	0.75	2.42	-26.70
QLS-52	Qinglongshan	Yinping	LSM	Shale	37.08	8.83	11.22	1.37	2.81	0.25	8.18	-24.71
QLS-54	Qinglongshan	Yinping	LSM	Shale	39.67	9.07	6.58	1.33	1.54	0.23	4.95	-24.31
QLS-56	Qinglongshan	Yinping	LSM	Shale	42.25	11.99	3.99	1.22	5.85	1.47	3.28	-25.09
QLS-58	Qinglongshan	Yinping	LSM	Shale	45.26	11.54	5.38	1.30	5.34	0.99	4.15	-24.60
QLS-59	Qinglongshan	Yinping	LSM	Shale	46.99	10.74	2.91	1.49	4.20	1.45	1.96	-24.87

Table S2 Quantitative distribution of various palynofacies particles recorded from PDS section, QLS section, and GD core

Sample	Amorphous organic matter	Phytoclasts	Palynomorphs
CSC-P1q-1	93.00	7.00	0.00
CSC-P2g-5	81.00	19.00	0.00
CSC-P2g-13	79.00	21.00	0.00
CSC-P2g-24	88.00	12.00	0.00
CSC-P2g-40	86.00	14.00	0.00
CSC-P2g-56	86.00	14.00	0.00
CSC-P2g-68	83.00	17.00	0.00
CH-23	89.00	11.00	0.00
CH-38	90.00	10.00	0.00
CH-46	89.00	11.00	0.00
CH-57	91.00	9.00	0.00
CH-63	78.00	22.00	0.00
CH-67	84.00	16.00	0.00
CH-74	42.00	48.00	10.00
GS-15	53.00	41.00	6.00
QLS-5	98.00	2.00	0.00
QLS-14	97.00	3.00	0.00
QLS-17	96.00	4.00	0.00
QLS-20	91.00	9.00	0.00
QLS-24	86.00	14.00	0.00
QLS-29	45.00	55.00	0.00
QLS-35	73.00	27.00	0.00
QLS-41	83.00	17.00	0.00
QLS-47	92.00	8.00	0.00
QLS-52	67.00	33.00	0.00
QLS-58	51.00	42.00	7.00
GD-7	89.00	9.00	0.00
GD-17	82.00	18.00	0.00
GD1-37	91.00	9.00	0.00
GD1-68	81.00	19.00	0.00
GD1-84	56.00	41.00	3.00